FIG 2 Increase in cholangiocytes in the Pten::Keap1-Alb mouse livers. (A) Histological analysis of the livers. Results of Masson trichrome staining (a to h) and immunohistochemistry using the anti-CK19 antibody (i to l) at P15 are shown. PV, portal vein; CV, central vein. The scale bars correspond to 1 mm (a to d) and 200 μm (e to l). (B) Serum biochemical test, measuring markers for liver injury (ALT, AST, and LDH), TCHO, DBIL/TBIL ratio, and ALB at P15 (n = 8 to 27). *, $P < 0.05$; **, $P < 0.01$. Asterisks without brackets indicate the comparison with control mice.

and cholangiocytes in Pten::Keap1::R26R mice without *Albumin-Cre* (Pten::Keap1::R26R) were negative for LacZ staining (Fig. 3A and C), and the tubular structures with CK19-positive staining were not increased in these mice (Fig. 3E and G). This result indicates that Pten::Keap1 double-mutant cells contribute to cholangiocytes, suggesting that the differentiation or proliferation of cholangiocytes was promoted through the simultaneous disruption of *Pten* and *Keap1*.

Single-allele deletion of *Nrf2* delays but does not rescue the lethality of Pten::Keap1-Alb mice. Because the livers of Pten::

Keap1-Alb::Nrf2$^{+/-}$ mice showed mild fibrosis (Fig. 2Ad and h), we continued the observation of the mice together with those of other genotypes, except for Pten::Keap1-Alb mice, which died by 1 month of age (Fig. 4A; also Fig. 1B). Pten::Keap1-Alb::Nrf2$^{+/-}$ mice started dying after 2 months of age and exhibited progressive hepatomegaly until 7 months of age, by which time all the mice were dead (Fig. 4B and C). However, Pten::Keap1-Alb::Nrf2$^{-/-}$ mice survived the entire period of observation, as did the control, Pten-Alb, and Keap1-Alb mice (Fig. 4B). Pten::Keap1-Alb:: Nrf2$^{-/-}$ mice also exhibited slight hepatomegaly compared with
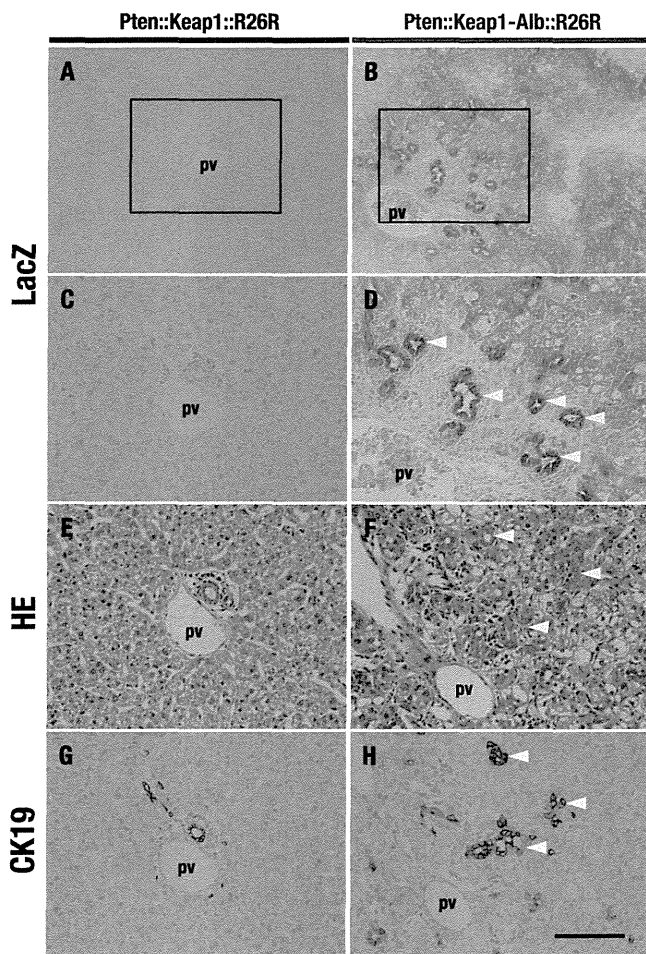
FIG 3 Expanded cholangiocytes are derived from *Pten* and *Keap1* doubly deficient cells. Liver sections of Pten::Keap::R26R and Pten::Keap1-Alb::R26R mice at P15 were subjected to LacZ staining (A to D), HE staining (E and F), and immunohistochemistry using the anti-CK19 antibody (G and H). Arrowheads indicate tubular structures of cholangiocytes. pv, portal vein. The scale bars correspond to 200 μm (A and B) and 100 μm (C to H).
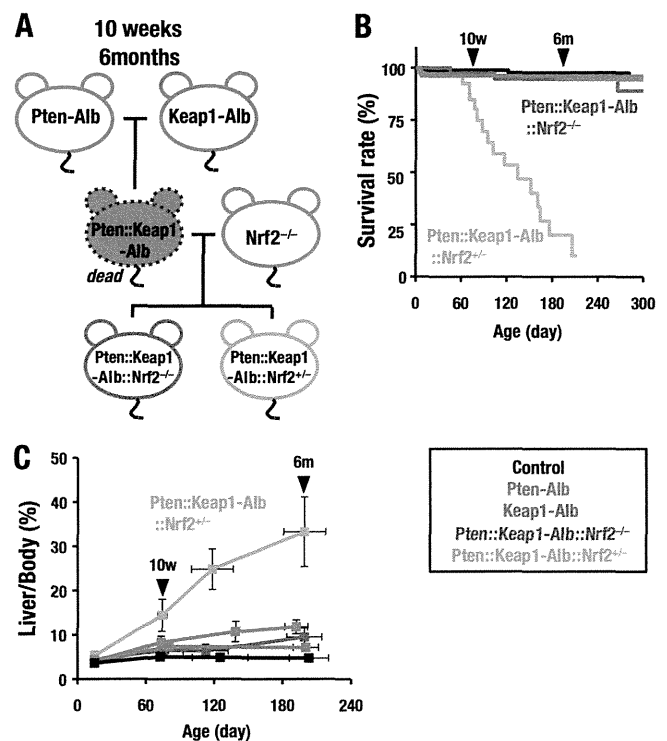

FIG 4 Pten::Keap1-Alb::Nrf2$^{+/-}$ mice demonstrate progressive hepatomegaly and die by 7 months of age. (A) Compound mutant mice of *Pten*, *Keap1*, and *Nrf2* genes analyzed at 10 weeks. Pten::Keap1-Alb mice that were lethal by 1 month were not included. (B) Survival rates at up to 240 days after birth ($n \geq 50$). (C) Changes in the liver-to-body-weight ratios up to 240 days ($n = 2$ to 43).

control mice, but the magnitude of the hepatomegaly was comparable to that of Pten-Alb and Keap1-Alb mice (Fig. 4C).

Cholangiocyte expansion is apparent in Pten::Keap1-Alb::Nrf2$^{+/-}$ liver at 10 weeks. At 10 weeks of age, female and male Pten-Alb mice exhibited a slight but significant increase in their liver-to-body-weight ratios (Fig. 5A, red bars), consistent with a previous report that Pten-Alb mice develop steatosis after 10 weeks (18). Keap1-Alb mice also displayed an increase in the ratio to a similar extent (Fig. 5A, light blue bars). In contrast, Pten::Keap1-Alb::Nrf2$^{+/-}$ mice, both female and male, showed dramatically increased liver-to-body-weight ratios at 10 weeks of age (Fig. 5A, light green bars), whereas Pten::Keap1-Alb::Nrf2$^{-/-}$ mice did not show any significant hepatomegaly (Fig. 5A, dark green bars). Surprisingly, Pten::Keap1-Alb::Nrf2$^{+/-}$ mice displayed the abnormal cholangiocyte expansion near the hepatic triad at 10 weeks (Fig. 5Be, j, and o), which was completely absent in control (Fig. 5Ba, f, and k), Pten-Alb (Fig. 5Bb, g, and l), and Keap1-Alb (Fig. 5Bc, h, and m) mice. Interestingly, mild expansion of cholangiocytes was observed in Pten::Keap1-Alb::Nrf2$^{-/-}$ mice (Fig. 5Bd, i, and n), implying the presence of an Nrf2-independent factor that promotes cholangiocyte expansion.

Pten::Keap1-Alb::Nrf2$^{+/-}$ mice develop polycystic liver fibrosis. In mice at 6 months of age, the appearance of Pten::Keap1-Alb::Nrf2$^{+/-}$ liver was dramatic. The Pten::Keap1-Alb::Nrf2$^{+/-}$ liver was significantly enlarged with a reddish brown color (Fig. 6A). Closer observation of the Pten::Keap1-Alb::Nrf2$^{+/-}$ liver revealed a multiple cystic appearance, and polycystic structures were confirmed in a section of the liver (Fig. 6B). CK19-positive tubular structures with fibrotic interstitial tissues occupied large portions of liver of Pten::Keap1-Alb::Nrf2$^{+/-}$ mice (Fig. 6Ce, j, and o), while healthy hepatocytes were hardly detected. In Pten::Keap1-Alb::Nrf2$^{+/-}$ mice, there were no signs of steatosis or carcinogenesis, which was different from our initial expectation.

In contrast, the livers of Pten-Alb mice and Pten::Keap1-Alb::Nrf2$^{-/-}$ mice did not develop any tumors but were whitish and slightly enlarged compared with control and Keap1-Alb livers (Fig. 6A). The histological analysis revealed severe steatosis in the pericentral vein area in Pten-Alb (Fig. 6Cb, g, and l) and Pten::Keap1-Alb::Nrf2$^{-/-}$ livers (Fig. 6Cd, i, and n), which was not observed in control (Fig. 6Ca, f, and k), Keap1-Alb (Fig. 6Cc, h, and m), or Pten::Keap1-Alb::Nrf2$^{+/-}$ (Fig. 6Ce, j, and o) livers. The mild expansion of cholangiocytes in Pten::Keap1-Alb::Nrf2$^{-/-}$ livers progressed at 6 months compared with 10 weeks (Fig. 6Cd, i, and n), but the severity was far less than the cholangiocyte expansion observed in Pten::Keap1-Alb::Nrf2$^{+/-}$ mice (Fig. 6Ce, j, and o), indicating that Nrf2 is the most critical factor in the progressive expansion of tubular structures lined with cholangiocytes. We surmise that an alternative substrate of Keap1 is responsible for the Nrf2-independent cholangiocyte expansion.
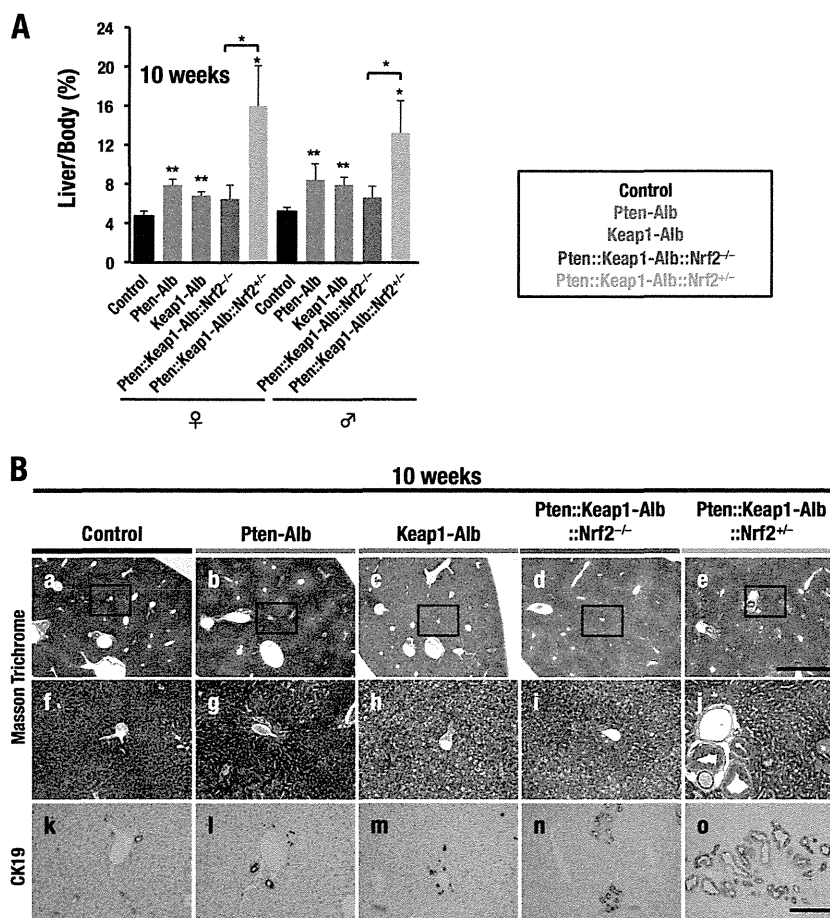
A

B

FIG 5 Cholangiocytes expansion in Pten::Keap1-Alb::Nrf2$^{+/-}$ mouse livers at 10 weeks. (A) Liver-to-body-weight ratios at 10 weeks (n = 3 to 10). More than 3 mice were independently examined for males and females of each genotype. $*$, $P < 0.05$; $**$, $P < 0.01$. Asterisks without brackets indicate the comparison with control mice. (B) Histological analysis of the livers at 10 weeks. Masson trichrome staining (a to j) and immunohistochemistry using the anti-CK19 antibody (k to o) are shown. The scale bars correspond to 1 mm (a to e) and 200 μm (f to o).

Gene expression profiles in Pten::Keap1-Alb mouse livers. To address the molecular mechanisms underlying cholangiocyte expansion, we performed a microarray analysis of Pten::Keap1-Alb, control, Keap1-Alb, and Pten-Alb mouse livers at P15. To delineate the Nrf2 dependency of the cholangiocyte expansion, we also conducted microarray analysis using Pten::Keap1-Alb:: Nrf2$^{-/-}$ mouse livers. Consistent with the results of the pathological analyses, the majority of cholangiocyte-specific or oval cell/liver progenitor cell (LPC)-specific gene markers were dramatically upregulated in Pten::Keap1-Alb mice compared with control, Keap1-Alb, or Pten-Alb mouse livers (Fig. 7). However, hepatocyte-specific gene markers were decreased in Pten::Keap1-Alb livers.

This upregulation of cholangiocyte or LPC-specific gene markers in Pten::Keap1-Alb mouse livers was mostly cancelled in Pten:: Keap1-Alb::Nrf2$^{-/-}$ mouse livers. Similarly, the expression of hepatocyte-specific genes was recovered in Pten::Keap1-Alb:: Nrf2$^{-/-}$ mouse livers. These results indicate that the upregulation of cholangiocyte-specific genes and downregulation of hepatocyte-specific genes in Pten::Keap1-Alb mouse livers reflect an increase in Nrf2.

Nrf2 activation contributes to the emergence of Trop2-EpCAM double-positive cells in Pten::Keap1-Alb mouse livers.

To validate the results of the microarray analyses, we then performed real-time quantitative PCR. Consistent with the results of the microarray analyses, expression of the cholangiocyte genes, including *Krt19*, *Ggt1*, and *Spp1*, was also increased in Pten:: Keap1-Alb mice (Fig. 8A). The increase was significantly abrogated in Pten::Keap1-Alb::Nrf2$^{-/-}$ mice. Conversely, expression of the hepatocyte genes, including *Alb* and *G6pc*, was indeed decreased in Pten::Keap1-Alb mice, and this decrease in hepatocyte gene expression was abrogated by the simultaneous disruption of *Nrf2* (Fig. 8B). These results further support the conclusion that increased Nrf2 activity and the loss of Pten activity contribute to the cholangiocyte expansion and the relative decrease in the hepatocyte population in the Pten::Keap1-Alb mouse liver.

We observed that Trop2 (also referred to as *Tacstd2*) was highly and specifically expressed in the Pten::Keap1-Alb mouse liver (Fig. 7). Trop2 has been shown to be a marker for oval cells/LPCs (32). We confirmed a 6-fold increase in *Trop2* expression specifically in the Pten::Keap1-Alb mouse liver using real-time quantitative PCR (Fig. 8C).

To examine whether oval cells emerged, we conducted immunofluorescent detection of Trop2 and EpCAM in the Pten::Keap1-Alb mouse liver. As EpCAM was expressed in both cholangiocytes and oval cells, we expected the emergence of Trop2-EpCAM double-pos-

A

6 months

B

Pten::Keap1-Alb::Nrf2+/-
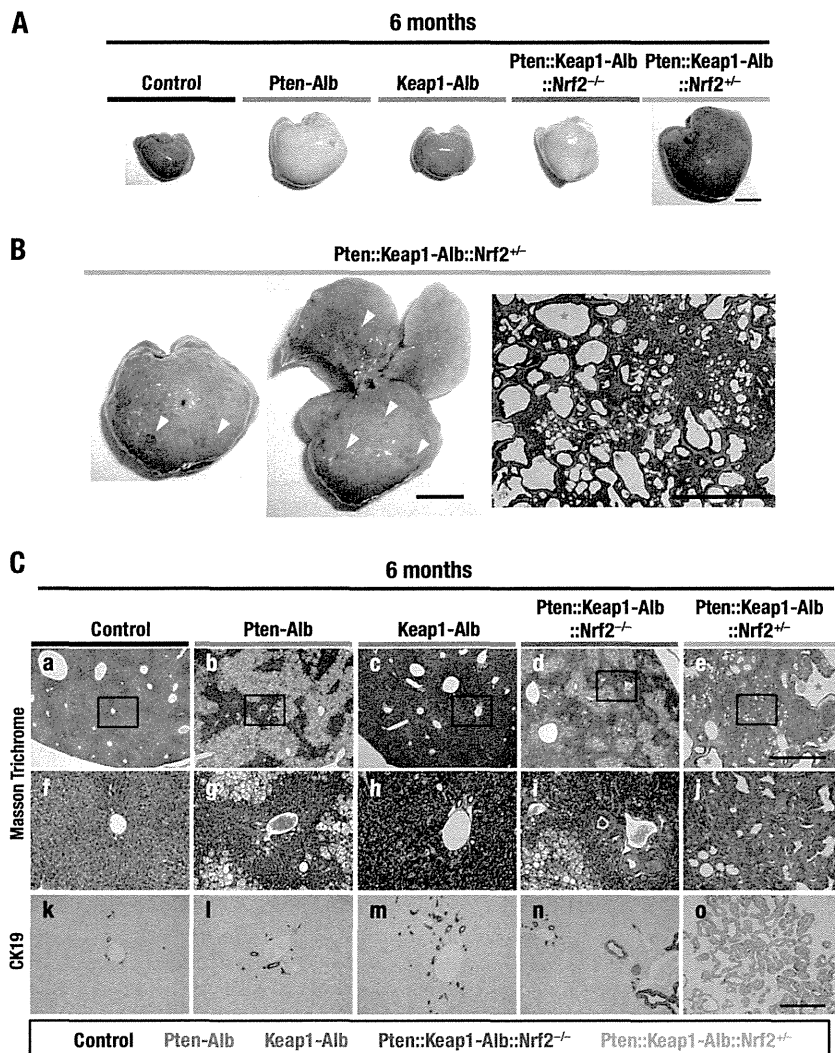

C

6 months

FIG 6 Development of polycystic fibrosis in Pten::Keap1-Alb::Nrf2$^{+/-}$ mice at the age of 6 months. (A) Representative macroscopic observation of the livers at 6 months of age. The scale bar corresponds to 1 cm. (B) Polycystic appearance of the Pten::Keap1-Alb::Nrf2$^{+/-}$ mouse liver in a closer view (left and middle panels) and in a section (right panel). Arrowheads indicate grossly recognizable cysts. A red asterisk indicates a cyst. The scale bars correspond to 1 cm (left and middle panels) and 1 mm (right panel). (C) Histological analysis of the livers at 6 months. Masson trichrome staining (a to j) and immunohistochemistry using the anti-CK19 antibody (k to o) are shown. The scale bars correspond to 1 mm (a to e) and 200 μm (f to o).

itive oval cells in the liver. The results revealed that a part of the cholangiocytes in Pten::Keap1-Alb mouse livers was indeed doubly positive for EpCAM and Trop2 (Fig. 8D). As oval cells have been reported to emerge in severely injured livers and contribute to the regeneration (32), these results imply that Nrf2 activation may induce oval cell expression and contribute to the abnormal expansion of cholangiocytes in Pten::Keap1-Alb mouse livers.

Enhanced phosphorylation of Gsk3 contributes to increased nuclear accumulation of Nrf2 in Pten::Keap1-Alb mice. Cholangiocyte lineage markers *Ggt1* and *Gstp1* have also been identified as typical Nrf2 target genes (33–36), and their expression levels were higher in Pten::Keap1-Alb mouse livers than in Keap1-Alb mouse livers (Fig. 7 and 8A). We observed that two other Nrf2 target genes, *Gpx2* and *Gclc*, showed similar expression patterns (Fig. 9A). The increased expression levels of *Gpx2* and *Gclc* mRNAs were completely abrogated by the concomitant deletion of *Nrf2*. These results are consistent with the notion that Nrf2-

dependent transcriptional activity was greatly enhanced in the Pten::Keap1-Alb liver through the increased nuclear accumulation of Nrf2 under conditions of sustained activation of the PI3K-Akt pathway (4). Indeed, when the nuclear extracts obtained from the livers of control, Pten-Alb, Keap1-Alb, and Pten::Keap1-Alb mice at P15 were examined, robust accumulation of Nrf2 protein was observed in the livers of Pten::Keap1-Alb mice compared with those of Keap1-Alb mice, accompanied by the increased expression of Nqo1 protein (Fig. 9B). The Nrf2 protein accumulation was not detectable in control and Pten-Alb mouse livers (Fig. 9B).

To understand the mechanisms underlying the increased Nrf2 accumulation in Pten::Keap1-Alb mouse livers, we examined the phosphorylation status of Gsk3 using liver protein extracts from control, Keap1-Alb, Pten-Alb, and Pten::Keap1-Alb mice. It has been shown that Gsk3, one of the main substrates of Akt, promotes Nrf2 degradation in an SCF/β-TrCP-dependent and Keap1-independent manner (37, 38). We observed that Gsk3 was

Cell type	Probe Name	Gene Symbol	Pten	Keap1	P::K	P::K::N	
Hepatocyte	A_51_P160713	Alb	-1.0	-1.1	-1.4	-1.1	albumin
	A_52_P251450	Cldn2	-1.1	1.4	-1.3	-1.2	claudin 2
	A_51_P266618	Cyp8b1	1.0	1.1	-2.5	-1.0	cytochrome P450, family 8, subfamily b, polypeptide 1
	A_51_P462385	G6pc	-1.1	1.1	-4.7	-1.0	glucose-6-phosphatase, catalytic
	A_52_P683991	Hnf4a	1.1	1.5	-1.2	1.5	hepatic nuclear factor 4, alpha
	A_52_P69656	Hnf4a	1.1	1.5	-1.1	1.2	hepatic nuclear factor 4, alpha
	A_51_P198473	Hnf4a	-1.1	1.2	-1.6	-1.5	hepatic nuclear factor 4, alpha
	A_51_P362638	Trf	1.1	1.0	-1.6	1.1	transferrin
Cholangiocyte	A_51_P155445	Abcb1a	1.2	-1.5	2.1	1.1	ATP-binding cassette, sub-family B (MDR/TAP), member 1A
	A_52_P92772	Abcb1b	1.2	-1.0	1.4	1.7	ATP-binding cassette, sub-family B (MDR/TAP), member 1B
	A_52_P170509	Abcb1b	-1.3	1.4	1.5	1.0	ATP-binding cassette, sub-family B (MDR/TAP), member 1B
	A_52_P245368	Abcb1b	-1.2	-1.2	2.1	-1.5	ATP-binding cassette, sub-family B (MDR/TAP), member 1B
	A_51_P500676	Dmbt1	2.3	43.4	18.5	2.1	deleted in malignant brain tumors 1
	A_52_P447944	Epcam	1.3	-1.3	8.1	-2.6	epithelial cell adhesion molecule
	A_51_P468073	Ggt1	1.3	31.6	258.8	1.2	gamma-glutamyltransferase 1
	A_51_P440238	Ggt6	-1.1	4.1	5.8	2.2	gamma-glutamyltransferase 6
	A_51_P374457	Gstp1	-1.2	3.3	2.4	-1.4	glutathione S-transferase, pi 1
	A_51_P374464	Gstp1	-1.1	4.2	5.8	-1.3	glutathione S-transferase, pi 1
	A_51_P484311	Hnf1b	-1.1	-1.3	-1.1	-1.5	HNF1 homeobox B
	A_52_P177699	Hnf1b	-1.0	1.0	1.3	-1.1	HNF1 homeobox B
	A_51_P312348	Krt7	1.1	1.6	17.1	1.2	keratin 7
	A_52_P410685	Krt7	1.2	1.3	14.4	1.1	keratin 7
	A_51_P356642	Krt19	1.2	2.2	13.5	1.1	keratin 19
	A_52_P214630	Sox9	1.1	1.2	7.4	-1.2	SRY-box containing gene 9
	A_51_P451606	Sox9	1.2	-1.0	4.5	-1.7	SRY-box containing gene 9
	A_52_P577484	Sox9	1.1	1.1	6.5	-1.9	SRY-box containing gene 9
	A_51_P358765	Spp1	1.7	1.1	14.2	-1.3	secreted phosphoprotein 1
	A_52_P190973	Vcl	1.0	1.3	2.3	-1.2	vinculin
	A_51_P297131	Vcl	-1.0	-1.0	1.9	-1.3	vinculin
Oval cell/Liver progenitor cell	A_52_P244193	Cd24a	1.2	1.2	6.9	1.4	CD24a antigen
	A_51_P257938	Tacstd2	3.5	-1.4	8.2	1.3	tumor-associated calcium signal transducer 2

Pten-Alb   Keap1-Alb   Pten::Keap1-Alb   Pten::Keap1-Alb::Nrf2^{-/-}

FIG 7 Expression of cell-specific marker genes in the liver at P15. Cell-specific gene markers were categorized into hepatocyte, cholangiocyte, and oval cell/liver progenitor cells in Pten-Alb, Keap1-Alb, Pten::Keap1-Alb, and Pten::Keap1-Alb::Nrf2$^{-/-}$ mouse livers at P15. The fold change values indicate the base 2 logarithm of the expression ratio to control mouse values.

markedly phosphorylated in Pten::Keap1-Alb mouse livers compared with control, Keap1-Alb, and Pten-Alb mouse livers (Fig. 9B). Because phosphorylated Gsk3 is inactive, these results suggest that Gsk3 phosphorylation under conditions of sustained activation of the PI3K-Akt pathway induces the increased accumulation of Nrf2. Thus, the massive accumulation of Nrf2 in Pten::Keap1-Alb livers is attributable to the simultaneous inactivation of the Keap1-dependent degradation and β-TrCP-dependent degradation of Nrf2.

Notably, Pten expression in Pten-Alb and Pten::Keap1-Alb mice was decreased but still detectable at P15, whereas Keap1 expression in Keap1-Alb and Pten::Keap1-Alb mice was almost undetectable (Fig. 9B). Therefore, to assess effects of complete Pten ablation on Nrf2 accumulation, we examined control and Pten-Alb mouse livers at the 10 weeks of age, when Pten was almost undetectable (Fig. 9B). At 10 weeks, Pten-Alb mouse livers exhibited the increased phosphorylation of Akt and Gsk3 but did not exhibit any Nrf2 accumulation above the control level. These results indicate that the β-TrCP-dependent degradation of Nrf2 is relatively minor for Nrf2 degradation compared with the Keap1 pathway. The contribution of the β-TrCP-dependent pathway to Nrf2 accumulation was detectible only when the Keap1 pathway was abrogated in the Pten::Keap1-Alb liver.

Moreover, we also examined the phosphorylation status of Akt and Gsk3 in the liver extracts from Pten::Keap1-Alb::Nrf2$^{-/-}$ mice compared with the phosphorylation status in those from Pten::Keap1-Alb mice. We observed a robust augmentation in Gsk3 phosphorylation in Pten::Keap1-Alb mouse livers, and this phosphorylation status was completely restored in Pten::Keap1-Alb::Nrf2$^{-/-}$ mouse livers (Fig. 9B). We also observed that the phosphorylation of Akt was significantly stimulated in the Pten::Keap1-Alb livers, and weak phosphorylation was observed in the absence of Nrf2 (Fig. 9B). These results are consistent with our previous observation that Nrf2 enhances the activity of the PI3K-Akt pathway (4), whose detailed mechanism remains to be elucidated.

DISCUSSION

This study revealed unique synthetic liver phenotypes driven by functional interactions between the Keap1-Nrf2 and Pten-PI3K-Akt pathways. The liver-specific double disruption of the *Pten* and *Keap1* genes results in dramatic hepatomegaly with expanded tubular structures comprising cholangiocytes and eventual periweaning lethality. Importantly, these abnormalities were all restored through the simultaneous disruption of *Nrf2*, indicating that the constitutive stabilization of Nrf2 in the liver under con-
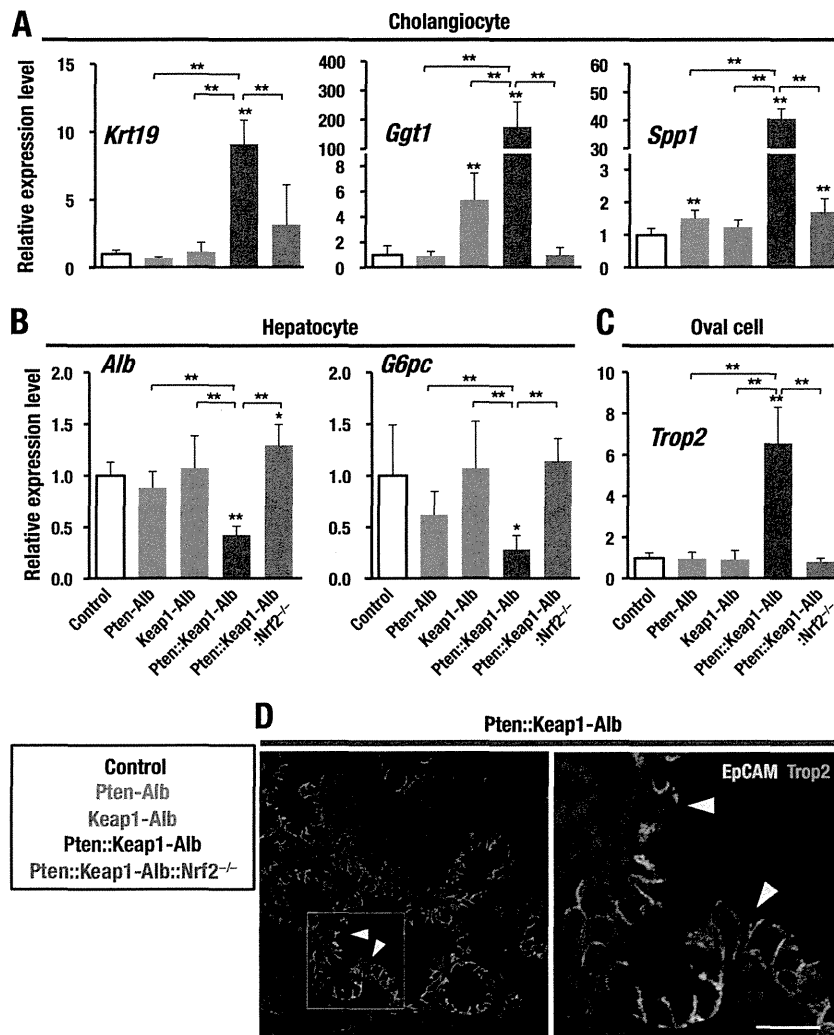
FIG 8 Gene expression profiles of Pten::Keap1-Alb liver. Relative expression of mRNAs in control, Pten-Alb, Keap1-Alb, Pten::Keap1-Alb, and Pten::Keap1-Alb::Nrf2$^{-/-}$ mouse livers of male mice at P15 ($n = 3$ to 6). The average values of control mice are set to 1. *, $P < 0.05$; **, $P < 0.01$. Asterisks without brackets indicate the comparison with control mice. The full gene names are listed in Fig. 7. (A) Expression levels of cholangiocyte-specific genes. (B) Expression levels of hepatocyte-specific genes. (C) Expression levels of oval cell-specific genes. (D) A representative immunofluorescent image of Pten::Keap1-Alb mouse livers using anti-EpCAM and anti-Trop2 antibodies. Higher magnification of the area surrounded by a white square is shown on the right. Arrowheads indicate the EpCAM-Trop2 double-positive cells. The scale bar corresponds to 50 µm (left panel) and 17 µm (right panel).

ditions of sustained activation of the PI3K-Akt pathway modulates cell growth and differentiation. Considering the well-characterized contribution of Nrf2 in response to stress, skewing cell lineage development is a particularly novel function of Nrf2 revealed in this study. We recently found another occasion where Nrf2 exerts the similar function, altering the lineage commitment of hematopoietic cells (52). Considering the wide-ranging expression of Nrf2, still other cell differentiation events may be under the control of Nrf2.

A characteristic histopathological feature of Pten::Keap1-Alb mice is the excessive expansion of cholangiocytes, which resembles the human pathology observed in liver cirrhosis, alcoholic liver injury, and acute hepatitis. Although the precise molecular mechanisms underlying the Nrf2-dependent expansion of cholangiocytes in Pten::Keap1-Alb mice are currently unknown, we speculate that Nrf2 promotes the differentiation of cholangiocytes at the stage of hepatoblasts on the basis of the observation

that *Pten* and *Keap1* gene disruption is initiated in hepatoblasts. It is also plausible that Nrf2 enhances the induction and differentiation of oval cells into cholangiocytes on the basis of the observation that Trop2-EpCAM double-positive cells, which are possible oval cells, are specifically induced in the livers of Pten::Keap1-Alb mice. Notably, similar phenotypes have been observed in the livers of *Fbxw7* conditional-knockout mice (39). The increased Notch pathway activity due to Fbxw7 deficiency skewed the differentiation of hepatoblasts toward the cholangiocyte lineage. In the present study, however, Notch pathway-related genes were generally not upregulated in the livers of Pten::Keap1-Alb mice, except for *Jag1* and *Hes1* (data not shown), suggesting that alternative mechanisms might operate in Pten::Keap1-Alb livers.

Another interesting histopathological alteration observed in Pten::Keap1-Alb mice is that involving liver fibrosis, especially in regions surrounding the increased cholangiocytes. It has been reported that Nrf2 activation suppresses hepatic fibrosis. For exam-
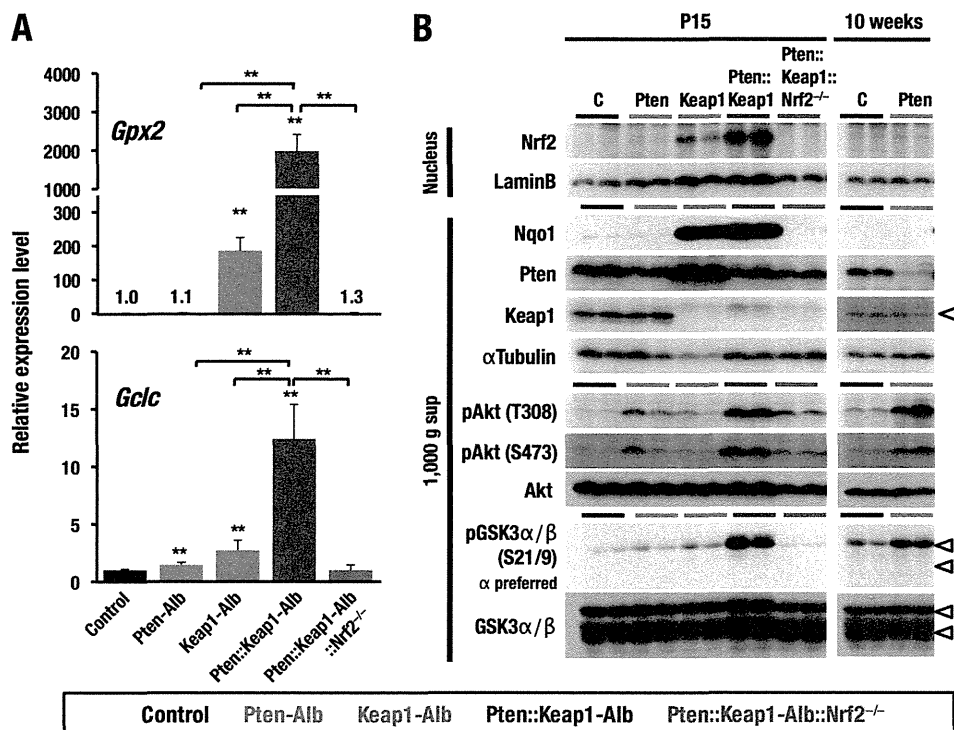
– 666 –

FIG 9 Enhancement of Nrf2 activity and the PI3K-Akt pathway in Pten::Keap1-Alb mouse livers. (A) Gene expression levels of representative Nrf2 target genes, *Gpx2* and *Gclc*, in control, Pten-Alb, Keap1-Alb, Pten::Keap1-Alb, and Pten::Keap1-Alb::Nrf2$^{-/-}$ mouse livers at P15 ($n = 3$ to 6). The average values of control mice are set to 1. *, $P < 0.05$; **, $P < 0.01$. Asterisks without brackets indicate the comparison with control mice. (B) Immunoblot analysis of liver extracts from control, Pten-Alb, Keap1-Alb, Pten::Keap1-Alb, and Pten::Keap1-Alb::Nrf2$^{-/-}$ mouse livers measuring the nuclear accumulation of Nrf2, reduction efficiency of Pten and Keap1, and phosphorylation of Akt and Gsk3. Nqo1 is the product of an Nrf2 target gene. Arrowheads indicate Keap1 and two isoforms of Gsk3. Control, Pten-Alb, Keap1-Alb, Pten::Keap1-Alb, and Pten::Keap1-Alb::Nrf2$^{-/-}$ mouse livers were analyzed at P15, and control and Pten-Alb mouse livers were also analyzed at 10 weeks.

ple, *Nrf2*-null mice fed a methionine- and choline-deficient diet exhibit steatohepatitis that is severer than that seen in wild-type mice (40). In such a case, fibrosis is preceded by steatosis and is considered secondary to liver damage. In contrast, our results indicate that Nrf2 activation seems to primarily promote fibrosis in the absence of Pten, because the fibrosis becomes evident prior to the cholangiocyte expansion in Pten::Keap1-Alb::Nrf2$^{+/-}$ mice. Importantly, steatosis is not detectable in either Pten::Keap1-Alb or Pten::Keap1-Alb::Nrf2$^{+/-}$ mice. Thus, the liver fibrosis observed in this study seems to be unique, as the pathology is not associated with steatosis.

In the present study, we clarified the relationship of two degradation systems which regulate Nrf2 abundance. The Keap1- and β-TrCP-dependent Nrf2 degradation pathways and their loss-of-function mutations are schematically shown in Fig. 10 (left and middle panels, respectively). Keap1 is an adaptor for Cul3-based ubiquitin ligase that is primarily located in the cytoplasm (26). The pathway involving Keap1-dependent ubiquitination and subsequent degradation of Nrf2 is the major regulatory pathway leading to the stabilization of Nrf2. In addition, the Keap1-independent degradation pathway, mediated through Cul1-based ubiquitin ligase, containing β-TrCP as an adaptor, has been reported (37, 38). Because this pathway requires the phosphorylation of Nrf2 by Gsk3, the β-TrCP-dependent degradation of Nrf2 is inhibited in the presence of the Pten deficiency, where Akt phosphorylates and inactivates Gsk3. Importantly, Nrf2 was not accumulated in Pten-Alb mice (Fig. 10, middle panel). In contrast, in

the presence of the double deficiency of the *Pten* and *Keap1* genes, where both degradation systems were inactivated, Nrf2 accumulation was dramatically increased (Fig. 10, right panel), indicating that the apparent contribution of β-TrCP-dependent degradation was observed only when the Keap1-dependent pathway was inactivated. Based on these observations, we propose that the β-TrCP-dependent mechanism contributes to the second-line degradation mechanism of Nrf2, which targets Nrf2 that has escaped from Keap1-dependent degradation. Because the β-TrCP-dependent mechanism has been implicated as a nuclear event (38), the Nrf2 that has escaped from the Keap1-dependent degradation in the cytoplasm is translocated into the nucleus and subjected to the β-TrCP-dependent degradation.

This study has substantiated two distinct Nrf2 degradation mechanisms operating *in vivo* and provided insights into the relationship between these two pathways. Based on accumulating lines of evidence, we have observed that cells adopt multilayered strategies for the Nrf2 activation/regulation. For instance, we discovered the electrophilic modification of Keap1 as a mechanism of Nrf2 stabilization/activation for the maintenance of redox homeostasis (3). We also observed that in human cancer cells, somatic mutations of the *KEAP1* or *NRF2* gene abrogate the KEAP1-mediated degradation of NRF2 (41, 42). The autophagy and mTOR pathways also critically contribute to Nrf2 activation (43, 44). In addition to Keap1-dependent regulation at the protein level, the transcriptional regulation of Nrf2 substantially influences Nrf2 activity (45, 46). Indeed, single nucleotide polymor-
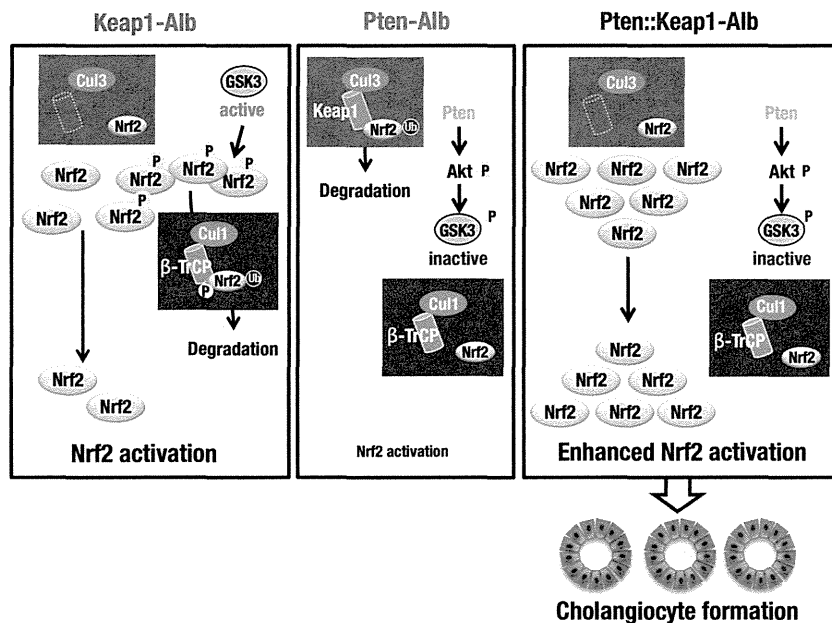
– 667 –

FIG 10 Two distinct pathways for Nrf2 degradation. Nrf2 is primarily degraded in a Keap1-Cul3-dependent manner. In Keap1-Alb mouse livers, Nrf2 escapes from the primary degradation but is subjected to secondary degradation mediated through β-TrCP-Cul1-dependent degradation, which limits Nrf2 accumulation. For secondary degradation, Nrf2 needs to be phosphorylated through Gsk3 (left panel). In Pten-Alb mouse livers, Gsk3 is inactivated but does not affect the Nrf2 abundance because the Keap1-Cul3-dependent pathway constantly degrades Nrf2 (middle panel). In Pten::Keap1-Alb mouse livers, Nrf2 escapes from primary and secondary degradation due to Keap1 deletion and Gsk3 inactivation, resulting in a robust increase of Nrf2 accumulation (right panel).

phisms in human *NRF2* and mouse *Nrf2* upstream-promoter regions alter the transcription levels of these genes, changing the overall activity of Nrf2 and its susceptibility to oxidative and xenobiotic insults. Of these layers of regulations, the β-TrCP-dependent degradation pathway is controlled through the PI3K-Akt signaling that has a profound influence on cell growth and differentiation. The PI3K-Akt pathway appears to regulate cell differentiation through Nrf2 activation under conditions that include the mitigation of Keap1-dependent degradation. Therefore, we propose that the coordinated sequential action of the Keap1- and β-TrCP-dependent degradation mechanisms forms a regulatory basis for the contribution of Nrf2 to cell lineage development.

The periweaning lethality of Pten::Keap1-Alb mice was one of the unexpected phenotypes obtained in the present study. The Pten::Keap1-Alb mice died before weaning, which was much earlier than the deaths of *Pten* or *Keap1* single-knockout mice. While we cannot identify any definitive causes of the periweaning death of the Pten::Keap1-Alb mice, we propose that the following observations might be pertinent. First, the gain in body weight of the Pten::Keap1-Alb mice was comparable to that of control mice, and the physical appearance of the mice was normal, except for mild abdominal swelling. Most of the Pten::Keap1-Alb mice died suddenly, without any apparent preceding signs. Second, we observed that the plasma levels of markers of liver injury in Pten::Keap1-Alb mice were higher than those in control mice but were not as high as those during fatal liver failure. The preliminary blood biochemistry analyses revealed that the UA level in plasma at P15 was three times higher in Pten::Keap1-Alb mice than in control mice but that the BUN score was elevated only mildly (data not shown). The elevated UA level in Pten::Keap1-Alb mice was decreased to the control level in Pten::Keap1-Alb::Nrf2$^{-/-}$ and Pten::Keap1-Alb::Nrf2$^{+/-}$ mice, showing a similar Nrf2 de-

pendency of the liver pathology and lethality. These wide-ranging observations suggest that the periweaning death of the Pten::Keap1-Alb mice might reflect a certain organ failure(s) provoked through liver-derived general metabolic changes rather than drastic developmental defects or severe liver injury.

Pten-Alb mice serve as unique models of nonalcoholic fatty liver disease, showing the stepwise progression from steatosis, steatohepatitis, and fibrosis to tumor formation (18). We were interested in the effect of Nrf2 activation on each stage of liver pathology in the *Pten*-null background, particularly on the transition from steatosis to steatohepatitis, as oxidative stress is one of the critical factors for the transition in Pten-Alb mouse livers (18). Indeed, previous reports described how Nrf2 contributes to protection of the liver in diet-associated steatosis models (40, 47). We predicted that Nrf2 activation through Keap1 disruption would reduce reactive oxygen species and prevent the development of steatohepatitis, even in the absence of Pten. Surprisingly, however, Nrf2 activation in the *Pten*-null background (Pten::Keap1-Alb:: Nrf2$^{+/-}$ mice) completely suppressed the development of not only steatohepatitis but also steatosis or lipid accumulation in hepatocytes at 6 months of age. In contrast, Nrf2-deficient (Pten:: Keap1-Alb::Nrf2$^{-/-}$) mouse livers exhibited steatosis similar to that observed in Pten-Alb mouse livers. Thus, these results demonstrate that the Nrf2 pathway antagonizes the increased synthesis and/or storage of triglycerides in hepatocytes caused by the Pten deficiency.

Another important phenotype of Pten deficiency is cancer developing from steatohepatitis in mice that are more than 12 months of age (18, 19). This long latency period suggests that genetic alterations need to accumulate to promote carcinogenesis. Because Nrf2 enhances the establishment of malignant cancers (13, 14), we initially anticipated that we would find that Nrf2

activation accelerates the oncogenic process through the Pten deficiency. In contrast to our expectation, however, Pten::Keap1-Alb::Nrf2$^{+/-}$ mice did not develop cancers but displayed noncancerous hepatomegaly with cholangiocyte expansion and eventual cystic liver fibrosis. Considering the cytoprotective function of Nrf2, we propose that Nrf2 stabilization might protect cells from the progressive accumulation of genetic mutations, resulting in the inhibition of the malignant transformation of cells. In contrast, the double deletion of *Pten* and *Smad4* in the liver develops cholangiocellular carcinoma after 4 months of age, which is much faster than that in Pten-Alb mice (19), indicating that the abrogation of transforming growth factor β (TGF-β) signaling promotes carcinogenesis. Thus, the functional contributions of the Nrf2 signaling to liver carcinogenesis are fundamentally distinct from those of TGF-β signaling.

In summary, the results of the present study showed that genetic Keap1 ablation/Nrf2 activation in Pten-deficient livers generates consequences in liver pathology that are completely different from those observed in singly Pten-deficient mice. The liver-specific Pten-Keap1 double disruption results in the dramatic hepatomegaly, with expanded tubular structures comprising cholangiocytes and eventual periweaning lethality. Notably, we identified, for the first time, that the massive expansion of Nrf2 in Pten-Keap1 double-knockout mice is induced through the simultaneous inactivation of two distinct Nrf2 degradation pathways. Thus, these results have established a new Nrf2-dependent molecular network that promotes cell proliferation and skews cell lineage development.

ACKNOWLEDGMENTS

REFERENCES

1. Motohashi H, Yamamoto M. 2004. Nrf2-Keap1 defines a physiologically important stress response mechanism. Trends Mol. Med. 10:549–557. http://dx.doi.org/10.1016/j.molmed.2004.09.003.
2. Hirotsu Y, Katsuoka F, Funayama R, Nagashima T, Nishida Y, Nakayama K, Engel JD, Yamamoto M. 2012. Nrf2-MafG heterodimers contribute globally to antioxidant and metabolic networks. Nucleic Acids Res. 40:10228–10239. http://dx.doi.org/10.1093/nar/gks827.
3. Kobayashi A, Kang MI, Watai Y, Tong KI, Shibata T, Uchida K, Yamamoto M. 2006. Oxidative and electrophilic stresses activate Nrf2 through inhibition of ubiquitination activity of Keap1. Mol. Cell. Biol. 26:221–229. http://dx.doi.org/10.1128/MCB.26.1.221-229.2006.
4. Mitsuishi Y, Taguchi K, Kawatani Y, Shibata T, Nukiwa T, Aburatani H, Yamamoto M, Motohashi H. 2012. Nrf2 redirects glucose and glutamine into anabolic pathways in metabolic reprogramming. Cancer Cell 22:66–79. http://dx.doi.org/10.1016/j.ccr.2012.05.016.
5. Singh A, Happel C, Manna SK, Acquaah-Mensah G, Carrerero J, Kumar S, Nasipuri P, Krausz KW, Wakabayashi N, Dewi R, Boros LG, Gonzalez FJ, Gabrielson E, Wong KK, Girnun G, Biswal S. 2013. Transcription factor NRF2 regulates miR-1 and miR-206 to drive tumorigenesis. J. Clin. Invest. 123:2921–2934. http://dx.doi.org/10.1172/JCI66353.
6. Taguchi K, Motohashi H, Yamamoto M. 2011. Molecular mechanisms of the Keap1-Nrf2 pathway in stress response and cancer evolution. Genes Cells 16:123–140. http://dx.doi.org/10.1111/j.1365-2443.2010.01473.x.
7. Inoue D, Suzuki T, Mitsuishi Y, Miki Y, Suzuki S, Sugawara S, Watanabe M, Sakurada A, Endo C, Uruno A, Sasano H, Nakagawa T, Satoh K, Tanaka N, Kubo H, Motohashi H, Yamamoto M. 2012. Accumulation of p62/SQSTM1 is associated with poor prognosis in patients with lung adenocarcinoma. Cancer Sci. 103:760–766. http://dx.doi.org/10.1111/j.1349-7006.2012.02216.x.
8. Mitsuishi Y, Motohashi H, Yamamoto M. 2012. The Keap1-Nrf2 system in cancers: stress response and anabolic metabolism. Front. Oncol. 2:200. http://dx.doi.org/10.3389/fonc.2012.00200.
9. Wakabayashi N, Itoh K, Wakabayashi J, Motohashi H, Noda S, Takahashi S, Imakado S, Kotsuji T, Otsuka F, Roop DR, Harada T, Engel JD, Yamamoto M. 2003. Keap1-null mutation leads to postnatal lethality due to constitutive Nrf2 activation. Nat. Genet. 35:238–245. http://dx.doi.org/10.1038/ng1248.
10. Motohashi H, Katsuoka F, Engel JD, Yamamoto M. 2004. Small Maf proteins serve as transcriptional cofactors for keratinocyte differentiation in the Keap1-Nrf2 regulatory pathway. Proc. Natl. Acad. Sci. U. S. A. 101:6379–6384. http://dx.doi.org/10.1073/pnas.0305902101.
11. Taguchi K, Maher JM, Suzuki T, Kawatani Y, Motohashi H, Yamamoto M. 2010. Genetic analysis of cytoprotective functions supported by graded expression of Keap1. Mol. Cell. Biol. 30:3016–3026. http://dx.doi.org/10.1128/MCB.01591-09.
12. Motohashi H, Fujita R, Takayama M, Inoue A, Katsuoka F, Bresnick EH, Yamamoto M. 2011. Molecular determinants for small Maf protein control of platelet production. Mol. Cell. Biol. 31:151–162. http://dx.doi.org/10.1128/MCB.00798-10.
13. Satoh H, Moriguchi T, Takai J, Ebina M, Yamamoto M. 2013. Nrf2 prevents initiation but accelerates progression through the Kras signaling pathway during lung carcinogenesis. Cancer Res. 73:4158–4168. http://dx.doi.org/10.1158/0008-5472.CAN-12-4499.
14. DeNicola GM, Karreth FA, Humpton TJ, Gopinathan A, Wei C, Frese K, Mangal D, Yu KH, Yeo CJ, Calhoun ES, Scrimieri F, Winter JM, Hruban RH, Iacobuzio-Donahue C, Kern SE, Blair IA, Tuveson DA. 2011. Oncogene-induced Nrf2 transcription promotes ROS detoxification and tumorigenesis. Nature 475:106–109. http://dx.doi.org/10.1038/nature10189.
15. Stambolic V, Suzuki A, de la Pompa JL, Brothers GM, Mirtsos C, Sasaki T, Ruland J, Penninger JM, Siderovski DP, Mak TW. 1998. Negative regulation of PKB/Akt-dependent cell survival by the tumor suppressor PTEN. Cell 95:29–39. http://dx.doi.org/10.1016/S0092-8674(00)81780-8.
16. Zhang S, Yu D. 2010. PI(3)king apart PTEN's role in cancer. Clin. Cancer Res. 16:4325–4330. http://dx.doi.org/10.1158/1078-0432.CCR-09-2990.
17. Hu TH, Huang CC, Lin PR, Chang HW, Ger LP, Lin YW, Changchien CS, Lee CM, Tai MH. 2003. Expression and prognostic role of tumor suppressor gene PTEN/MMAC1/TEP1 in hepatocellular carcinoma. Cancer 97:1929–1940. http://dx.doi.org/10.1002/cncr.11266.
18. Horie Y, Suzuki A, Kataoka E, Sasaki T, Hamada K, Sasaki J, Mizuno K, Hasegawa G, Kishimoto H, Iizuka M, Naito M, Enomoto K, Watanabe S, Mak TW, Nakano T. 2004. Hepatocyte-specific Pten deficiency results in steatohepatitis and hepatocellular carcinomas. J. Clin. Invest. 113:1774–1783. http://dx.doi.org/10.1172/JCI20513.
19. Xu X, Kobayashi S, Qiao W, Li C, Xiao C, Radaeva S, Stiles B, Wang RH, Ohara N, Yoshino T, LeRoith D, Torbenson MS, Gores GJ, Wu H, Gao B, Deng CX. 2006. Induction of intrahepatic cholangiocellular carcinoma by liver-specific disruption of Smad4 and Pten in mice. J. Clin. Invest. 116:1843–1852. http://dx.doi.org/10.1172/JCI27282.
20. Itoh K, Chiba T, Takahashi S, Ishii T, Igarashi K, Katoh Y, Oyake T, Hayashi N, Satoh K, Hatayama I, Yamamoto M, Nabeshima Y. 1997. An Nrf2/small Maf heterodimer mediates the induction of phase II detoxifying enzyme genes through antioxidant response elements. Biochem. Biophys. Res. Commun. 236:313–322. http://dx.doi.org/10.1006/bbrc.1997.6943.
21. Okawa H, Motohashi H, Kobayashi A, Aburatani H, Kensler TW, Yamamoto M. 2006. Hepatocyte-specific deletion of the keap1 gene activates Nrf2 and confers potent resistance against acute drug toxicity. Biochem. Biophys. Res. Commun. 339:79–88. http://dx.doi.org/10.1016/j.bbrc.2005.10.185.
22. Postic C, Magnuson MA. 2000. DNA excision in liver by an albumin-Cre transgene occurs progressively with age. Genesis 26:149–150. http://dx.doi.org/10.1002/(SICI)1526-968X(200002)26:2<149::AID-GENE16>3.0.CO;2-V.

23. Soriano P. 1999. Generalized lacZ expression with the ROSA26 Cre reporter strain. Nat. Genet. 21:70–71. http://dx.doi.org/10.1038/5007.

24. Mura C, Le Gac G, Jacolot S, Ferec C. 2004. Transcriptional regulation of the human HFE gene indicates high liver expression and erythropoiesis coregulation. FASEB J. 18:1922–1924. http://dx.doi.org/10.1096/fj.04 -2520fje.

25. Maruyama A, Tsukamoto S, Nishikawa K, Yoshida A, Harada N, Motojima K, Ishii T, Nakane A, Yamamoto M, Itoh K. 2008. Nrf2 regulates the alternative first exons of CD36 in macrophages through specific antioxidant response elements. Arch. Biochem. Biophys. 477:139–145. http://dx.doi.org/10.1016/j.abb.2008.06.004.

26. Watai Y, Kobayashi A, Nagase H, Mizukami M, McEvoy J, Singer JD, Itoh K, Yamamoto M. 2007. Subcellular localization and cytoplasmic complex status of endogenous Keap1. Genes Cells 12:1163–1178. http://dx.doi.org/10.1111/j.1365-2443.2007.01118.x.

27. Yamamoto T, Suzuki T, Kobayashi A, Wakabayashi J, Maher J, Motohashi H, Yamamoto M. 2008. Physiological significance of reactive cysteine residues of Keap1 in determining Nrf2 activity. Mol. Cell. Biol. 28:2758–2770. http://dx.doi.org/10.1128/MCB.01704-07.

28. Tanimizu N, Nishikawa M, Saito H, Tsujimura T, Miyajima A. 2003. Isolation of hepatoblasts based on the expression of Dlk/Pref-1. J. Cell Sci. 116:1775–1786. http://dx.doi.org/10.1242/jcs.00388.

29. Tanaka M, Miyajima A. 2012. Identification and isolation of adult liver stem/progenitor cells. Methods Mol. Biol. 826:25–32. http://dx.doi.org/10 .1007/978-1-61779-468-1_3.

30. Onodera K, Takahashi S, Nishimura S, Ohta J, Motohashi H, Yomogida K, Hayashi N, Engel JD, Yamamoto M. 1997. GATA-1 transcription is controlled by distinct regulatory mechanisms during primitive and definitive erythropoiesis. Proc. Natl. Acad. Sci. U. S. A. 94:4487–4492. http://dx .doi.org/10.1073/pnas.94.9.4487.

31. Tanimizu N, Miyajima A. 2004. Notch signaling controls hepatoblast differentiation by altering the expression of liver-enriched transcription factors. J. Cell Sci. 117:3165–3174. http://dx.doi.org/10.1242/jcs.01169.

32. Okabe M, Tsukahara Y, Tanaka M, Suzuki K, Saito S, Kamiya Y, Tsujimura T, Nakamura K, Miyajima A. 2009. Potential hepatic stem cells reside in EpCAM+ cells of normal and injured mouse liver. Development 136:1951–1960. http://dx.doi.org/10.1242/dev.031369.

33. Caperna TJ, Blomberg le, Garrett AWM, Talbot NC. 2011. Culture of porcine hepatocytes or bile duct epithelial cells by inductive serum-free media. In Vitro Cell Dev. Biol. Anim. 47:218–233. http://dx.doi.org/10 .1007/s11626-010-9382-3.

34. Zhang H, Liu H, Dickinson DA, Liu RM, Postlethwait EM, Laperche Y, Forman HJ. 2006. gamma-Glutamyl transpeptidase is induced by 4-hydroxynonenal via EpRE/Nrf2 signaling in rat epithelial type II cells. Free Radic. Biol. Med. 40:1281–1292. http://dx.doi.org/10.1016/j.freeradbiomed .2005.11.005.

35. Usami H, Kusano Y, Kumagai T, Osada S, Itoh K, Kobayashi A, Yamamoto M, Uchida K. 2005. Selective induction of the tumor marker glutathione S-transferase P1 by proteasome inhibitors. J. Biol. Chem. 280:25267–25276. http://dx.doi.org/10.1074/jbc.M501014200.

36. Tee LB, Kirilak Y, Huang WH, Smith PG, Morgan RH, Yeoh GC. 1996. Dual phenotypic expression of hepatocytes and bile ductular markers in developing and preneoplastic rat liver. Carcinogenesis 17:251–259. http://dx.doi.org/10.1093/carcin/17.2.251.

37. Rada P, Rojo AI, Chowdhry S, McMahon M, Hayes JD, Cuadrado A. 2011. SCF/{beta}-TrCP promotes glycogen synthase kinase 3-dependent degradation of the Nrf2 transcription factor in a Keap1-independent manner. Mol. Cell. Biol. 31:1121–1133. http://dx.doi.org/10.1128/MCB .01204-10.

38. Chowdhry S, Zhang Y, McMahon M, Sutherland C, Cuadrado A, Hayes JD. 2013. Nrf2 is controlled by two distinct beta-TrCP recognition motifs in its Neh6 domain, one of which can be modulated by GSK-3 activity. Oncogene 32:3765–3781. http://dx.doi.org/10.1038/onc.2012.388.

39. Onoyama I, Suzuki A, Matsumoto A, Tomita K, Katagiri H, Oike Y, Nakayama K, Nakayama KI. 2011. Fbxw7 regulates lipid metabolism and cell fate decisions in the mouse liver. J. Clin. Invest. 121:342–354. http://dx .doi.org/10.1172/JCI40725.

40. Sugimoto H, Okada K, Shoda J, Warabi E, Ishige K, Ueda T, Taguchi K, Yanagawa T, Nakahara A, Hyodo I, Ishii T, Yamamoto M. 2010. Deletion of nuclear factor-E2-related factor-2 leads to rapid onset and progression of nutritional steatohepatitis in mice. Am. J. Physiol. Gastrointest. Liver Physiol. 298:G283–G294. http://dx.doi.org/10.1152/ajpgi .00296.2009.

41. Shibata T, Kokubu A, Gotoh M, Ojima H, Ohta T, Yamamoto M, Hirohashi S. 2008. Genetic alteration of Keap1 confers constitutive Nrf2 activation and resistance to chemotherapy in gallbladder cancer. Gastroenterology 135:1358–1368. http://dx.doi.org/10.1053/j.gastro.2008.06 .082.

42. Padmanabhan B, Tong KI, Ohta T, Nakamura Y, Scharlock M, Ohtsuji M, Kang MI, Kobayashi A, Yokoyama S, Yamamoto M. 2006. Structural basis for defects of Keap1 activity provoked by its point mutations in lung cancer. Mol. Cell 21:689–700. http://dx.doi.org/10.1016/j.molcel.2006.01 .013.

43. Komatsu M, Kurokawa H, Waguri S, Taguchi K, Kobayashi A, Ichimura Y, Sou YS, Ueno I, Sakamoto A, Tong KI, Kim M, Nishito Y, Iemura S, Natsume T, Ueno T, Kominami E, Motohashi H, Tanaka K, Yamamoto M. 2010. The selective autophagy substrate p62 activates the stress responsive transcription factor Nrf2 through inactivation of Keap1. Nat. Cell Biol. 12:213–223. http://dx.doi.org/10.1038/ncb2021.

44. Ichimura Y, Waguri S, Sou YS, Kageyama S, Hasegawa J, Ishimura R, Saito T, Yang Y, Kouno T, Fukutomi T, Hoshii T, Hirao A, Takagi K, Mizushima T, Motohashi H, Lee MS, Yoshimori T, Tanaka K, Yamamoto M, Komatsu M. 2013. Phosphorylation of p62 activates the Keap1-Nrf2 pathway during selective autophagy. Mol. Cell 51:618–631. http://dx.doi.org/10.1016/j.molcel.2013.08.003.

45. Suzuki T, Shibata T, Takaya K, Shiraishi K, Kohno T, Kunitoh H, Tsuta K, Furuta K, Goto K, Hosoda F, Sakamoto H, Motohashi H, Yamamoto M. 2013. Regulatory nexus of synthesis and degradation deciphers cellular Nrf2 expression levels. Mol. Cell. Biol. 33:2402–2412. http://dx.doi.org/10 .1128/MCB.00065-13.

46. Cho HY, Jedlicka AE, Reddy SP, Kensler TW, Yamamoto M, Zhang LY, Kleeberger SR. 2002. Role of NRF2 in protection against hyperoxic lung injury in mice. Am. J. Respir. Cell Mol. Biol. 26:175–182. http://dx.doi.org /10.1165/ajrcmb.26.2.4501.

47. Wang C, Cui Y, Li C, Zhang Y, Xu S, Li X, Li H, Zhang X. 2013. Nrf2 deletion causes "benign" simple steatosis to develop into nonalcoholic steatohepatitis in mice fed a high-fat diet. Lipids Health Dis. 12:165. http://dx.doi.org/10.1186/1476-511X-12-165.

48. Kennedy AR, Pissios P, Otu H, Roberson R, Xue B, Asakura K, Furukawa N, Marino FE, Liu FF, Kahn BB, Libermann TA, Maratos-Flier E. 2007. A high-fat, ketogenic diet induces a unique metabolic state in mice. Am. J. Physiol. Endocrinol. Metab. 292:E1724–E1739. http://dx .doi.org/10.1152/ajpendo.00717.2006.

49. Zhong B, Zhou Q, Toivola DM, Tao GZ, Resurreccion EZ, Omary MB. 2004. Organ-specific stress induces mouse pancreatic keratin overexpression in association with NF-kappaB activation. J. Cell Sci. 117:1709–1719. http://dx.doi.org/10.1242/jcs.01016.

50. Takamura A, Komatsu M, Hara T, Sakamoto A, Kishi C, Waguri S, Eishi Y, Hino O, Tanaka K, Mizushima N. 2011. Autophagy-deficient mice develop multiple liver tumors. Genes Dev. 25:795–800. http://dx.doi .org/10.1101/gad.2016211.

51. Cole SE, Wiltshire T, Rue EE, Morrow D, Hieter P, Brahe C, Fisher EM, Katsanis N, Reeves RH. 1999. High-resolution comparative physical mapping of mouse chromosome 10 in the region of homology with human chromosome 21. Mamm. Genome 10:229–234. http://dx.doi.org/10 .1007/s003359900978.

52. Murakami S, Shimizu R, Romeo P-H, Yamamoto M, Motohashi H. Keap1-Nrf2 system regulates cell fate determination of hematopoietic stem cells. Genes Cells, in press.

−670−

Deficiency of Oncostatin M Receptor β (OSMRβ) Exacerbates High-fat Diet-induced Obesity and Related Metabolic Disorders in Mice*

Tadasuke Komori[‡], Minoru Tanaka[§], Emiko Senba[‡], Atsushi Miyajima[§], and Yoshihiro Morikawa[‡1]

From the ‡Department of Anatomy and Neurobiology, Wakayama Medical University, Wakayama 641-8509, Japan and §Laboratory of Cell Growth and Differentiation, Institute of Molecular and Cellular Biosciences, The University of Tokyo, Tokyo 113-0032, Japan

Background: Obesity is associated with adipose tissue inflammation, insulin resistance, and hepatic steatosis.
Results: OSM receptor β (OSMRβ)-deficient mice fed a high-fat diet exhibited severe obesity, adipose tissue inflammation, insulin resistance, and hepatic steatosis.
Conclusion: OSM signaling has suppressive effects on the deterioration of obesity-induced metabolic disorders.
Significance: These results indicate that OSM signaling may be a promising therapeutic target of obesity-induced metabolic disorders.

Oncostatin M (OSM) belongs to the IL-6 family of cytokines and has diverse biological effects, including the modulation of inflammatory responses. In the present study we analyzed the roles of OSM signaling in obesity and related metabolic disorders. Under a high-fat diet condition, OSM receptor β subunit-deficient (OSMRβ$^{-/-}$) mice exhibited increases in body weight and food intake compared with those observed in WT mice. In addition, adipose tissue inflammation, insulin resistance, and hepatic steatosis were more severe in OSMRβ$^{-/-}$ mice than in wild-type (WT) mice. These metabolic phenotypes did not improve when OSMRβ$^{-/-}$ mice were pair-fed with WT mice, suggesting that the effects of OSM signaling on these phenotypes are independent of the increases in the body weight and food intake. In the liver of OSMRβ$^{-/-}$ mice, the insulin-induced phosphorylation of p70 S6 kinase remained intact, whereas insulin-induced FOXO1 phosphorylation was impaired. In addition, OSMRβ$^{-/-}$ mice displayed a higher expression of genes related to de novo lipogenesis in the liver than WT mice. Furthermore, treatment of genetically obese ob/ob mice with OSM improved insulin resistance, adipose tissue inflammation, and hepatic steatosis. Intraportal administration of OSM into ob/ob mice activated STAT3 and increased the expression of long-chain acyl-CoA synthetase (ACSL) 3 and ACSL5 with decreased expression of fatty acid synthase in the liver, suggesting that OSM directly induces lipolysis and suppresses lipogenesis in the liver of obese mice. These findings suggest that defects in OSM signaling promote the deterioration of high-fat diet-induced obesity and related metabolic disorders.

Obesity-induced insulin resistance is known to be a strong risk factor for the development of type 2 diabetes and subse-quent cardiovascular disease (1). In the past decade it has been reported that obesity is underlying chronic low-grade inflammation that causes various metabolic disorders, including insulin resistance (2). Under obese conditions, a variety of inflammatory cells, including macrophages, neutrophils, T-cells, and eosinophils, are activated, stimulating infiltration, in adipose tissue (3–6). Among these inflammatory cells, classically activated macrophages (M1-type macrophages) in adipose tissue secrete proinflammatory cytokines (TNF-α and IL-1β), which induce insulin resistance (7–11). In contrast, adipose tissue in non-obese animals predominantly contains alternatively activated macrophages (M2-type macrophages) that suppress inflammation by producing anti-inflammatory cytokines, such as IL-10 (12, 13). Therefore, obesity stimulates a switch in the macrophage phenotype in adipose tissue toward the M1-type, which plays an important role in the attenuation of insulin sensitivity. However, the mechanisms underlying the development of obesity-induced adipose tissue inflammation and insulin resistance are not fully understood.

Oncostatin M (OSM)[2] is a member of the IL-6 family of cytokines, including IL-6, IL-11, leukemia inhibitory factor, ciliary neurotrophic factor, and cardiotrophin-1 (14). OSM exerts a variety of biological effects depending on the target cell by binding to the heterodimeric membrane receptor comprising the OSM specific β subunit (OSMRβ) and gp130 (15). It has been reported that OSM is produced by inflammatory cells, such as activated T cells, neutrophils, eosinophils, and macrophages (16–18), and is associated with many inflammatory diseases, including lung inflammation, rheumatoid arthritis, and multi-

---

[1] To whom correspondence should be addressed. Dept. of Anatomy and Neurobiology, Wakayama Medical University, 811-1 Kimiidera, Wakayama 641-8509, Japan. Tel.: and Fax: 81-73-441-0617; E-mail: yoshim@wakayama-med.ac.jp.

[2] The abbreviations used are: OSM, oncostatin M; OSMRβ, OSM-specific β subunit; OSMRβ$^{-/-}$, OSMRβ-deficient; ATM, adipose tissue macrophage; AUC, areas under the curve; DIO, diet-induced obese; HFD, high-fat diet; ipGTT, intraperitoneal glucose tolerance test; ITT, insulin tolerance test; RT, room temperature; MCP-1, monocyte chemoattractant protein-1; CCR2, C-C chemokine receptor 2; TLR4, toll-like receptor 4; FAS, fatty-acid synthase; SCD-1, stearoyl CoA desaturase-1; SREBF-1, sterol regulatory-element binding transcription factor-1; PF, pair-fed; PAS, periodic acid-Schiff; SVF, stromal vascular fraction; S6K, S6 kinase.

−671−

ple sclerosis (19, 20). In a previous study we reported that OSMRβ is expressed in adipose tissue macrophages (ATMs) and that OSM switches the phenotype of ATMs from the M1-type to the M2-type (21). In addition, disruption of OSMRβ gene in mice results in the development of mature-onset obesity and systemic insulin resistance under normal dietary conditions (21). However, the role of OSM signaling in the regulation of diet-induced obesity and related metabolic disorders remains unclear. In the present study we analyzed metabolic parameters in OSMRβ$^{-/-}$ mice fed a high-fat diet (HFD) to investigate the role of OSM signaling in the development of obesity-induced metabolic disorders, including adipose tissue inflammation, insulin resistance, and hepatic steatosis.

EXPERIMENTAL PROCEDURES

Animals—Male C57BL/6J mice (8 weeks old) were purchased from Nihon SLC (Hamamatsu, Japan). Male +/+ (lean) and *ob/ob* mice (8 weeks old) were obtained from our breeding colony using heterozygous (*ob/+*) breeding pairs. The protocol used to generate OSMRβ$^{-/-}$ mice has been described previously (22). OSMRβ$^{+/+}$ wild-type (WT) and OSMRβ$^{-/-}$ littermates were obtained from our breeding colony using heterozygous (+/−) breeding pairs. All mice were housed in specific pathogen-free facilities and light (12-h light/dark cycle)-, temperature (22–25 °C)-, and humidity (50–60% relative humidity)-controlled conditions. The mice were allowed free access to food and water. Until 8 weeks of age, all mice were fed a normal diet consisting of 13.3% calories from fat (MF; Oriental Yeast, Tokyo, Japan). At all times the experiments were performed under the control of the Animal Research Control Committee in accordance with the Guidelines for Animal Experiments of Wakayama Medical University, Japanese Government Notification on Feeding and Safekeeping of Animals (no. 6) and National Institutes of Health Guide for the Care and Use of Laboratory Animals (NIH publication no. 80–23, revised 1978). All efforts were made to minimize the number of animals used and their suffering.

HFD—Diet-induced obese (DIO) mice were generated by placing male C57BL/6J mice on an HFD consisting of 56.7% of calories from fat (High Fat Diet 32; CLEA Japan, Tokyo, Japan) beginning at 8 weeks of age for 8 weeks. OSMRβ$^{-/-}$ mice and their littermates were placed on the HFD starting at 8 weeks of age and fed in individual cages for 2, 4, or 8 weeks.

Pair-feeding on the HFD—Pair-feeding study was performed with some modifications as described by Racioppi *et al.* (23). WT and OSMRβ$^{-/-}$ mice at 8 weeks of age were housed in individual cages. The amount of food intake for the WT mice fed *ad libitum* and OSMRβ$^{-/-}$ mice fed *ad libitum* was monitored daily for the duration of the experiment. As OSMRβ$^{-/-}$ mice fed *ad libitum* would eat more food than WT mice fed *ad libitum*, OSMRβ$^{-/-}$ mice received the average amount of food consumed by the WT mice. All mice had free access to water. The food was provided to mice every day at 18:00, 2 h before the dark period began. Pair-feeding was carried out for 8 weeks. Body weights were recorded once a week throughout the experiment.

Injection of OSM in ob/ob Mice—Injection of OSM was performed as described previously (21). Briefly, *ob/ob* mice were

administrated intraperitoneally with either vehicle or recombinant mouse OSM (12.5 ng/g of body weight; R & D Systems, Minneapolis, MN) twice a day (10:00 and 18:00 h) for 1 week.

Intraportal Administration of OSM in ob/ob Mice—To investigate the direct effects of OSM on the liver of obese mice, *ob/ob* mice were deeply anesthetized with isoflurane and administrated intraportally with either vehicle or recombinant mouse OSM (12.5 ng/g of body weight). After 15, 30, 60, or 120 min of administration, the livers were excised, and the tissue lysates were prepared as described below.

Isolation of the Adipocyte Fraction and Stromal Vascular Fraction (SVF)—Isolation of the adipocyte fraction and SVF was performed as previously described (21). The mice were deeply anesthetized with diethyl ether, and the epididymal adipose tissue was quickly removed. The adipose tissue was minced into fine pieces and digested with collagenase type 2 (Sigma) dissolved in PBS supplemented with 2% FCS at 37 °C for 20 min. Next, the samples were passed through a nylon mesh (100-μm pore size; BD Biosciences) and fractioned by brief centrifugation (1200 rpm) at room temperature (RT) for 5 min. Floating cells and pellets were collected as the adipocyte fraction and SVF, respectively. The cells in the SVF were incubated with ammonium chloride buffer (PharmLyse; BD Biosciences) to lyse the erythrocytes.

Flow Cytometry—Flow cytometry was performed as previously described (21). The cells in the SVF were incubated with anti-CD16/CD32 antibodies (1:100, BD Biosciences) to block Fc binding at 4 °C for 20 min. The cells were then incubated with the following primary antibodies at 4 °C for 30 min: fluorescein isothiocyanate-conjugated anti-F4/80 antibody (eBiosciences), phycoerythrin-conjugated anti-CD11c antibody (eBiosciences), and Alexa Fluor 647-conjugated anti-CD206 antibody (AbD Serotec). To detect OSMRβ in the SVF, cells were incubated with goat anti-OSMRβ antibody (diluted at 1:5, R&D Systems) at 4 °C for 30 min. Then, the cells were incubated with phycoerythrin-conjugated donkey anti-goat IgG (diluted at 1: 20, R&D Systems). The stained cells were analyzed using the C6 flow cytometer (BD Biosciences) or the FACSCalibur flow cytometer (BD Biosciences). The stained cells were analyzed using the C6 flow cytometer (Accuri Cytometers). Dead cells were removed from the analysis using propidium iodide staining. The flow cytometry results were analyzed using the FlowJo (Tree Star) software suite. The events were first gated based on a forward scatter plot *versus* propidium iodide to identify individual live cells. The plot of a forward- *versus* side-scatter pattern was used as the second gate to gate out aggregates and debris. The cells gated on the F4/80-positive population were then analyzed for CD11c, CD206, and OSMRβ. Single color controls were used to set the compensation and gates.

Insulin Signaling Analysis—An insulin signaling analysis was performed as previously described (21). To evaluate insulin signaling, mice fasted for 24 h were intraperitoneally injected with human insulin (10 milliunits/g of body weight). Ten minutes later epididymal adipose tissue, gastrocnemius muscle, and liver were excised and frozen in liquid nitrogen. Tissue lysates were prepared as described below.

Western Blot Analysis—Western blot analysis was performed with some modifications, as previously described (24). Tissue lysates were prepared using radioimmune precipitation assay buffer (Upstate Biotechnology) containing protease inhibitor mixture (Upstate Biotechnology), 1 mM orthovanadate, 1 mM sodium fluoride, and 1 mM phenylmethylsulfonyl fluoride. The protein concentrations in the lysates were determined using a BCA Protein Assay kit (Pierce). Twenty micrograms of protein obtained from the samples was separated by sodium dodecyl sulfate-polyacrylamide gel electrophoresis (SDS-PAGE) and transferred to PVDF membranes (GE Healthcare). The blotted membranes were incubated with goat anti-OSMRβ antibody (diluted 1:1000, R&D Systems), rabbit anti-phosphorylated Akt antibody (diluted at 1:1000, Cell Signaling Technology), rabbit anti-phosphorylated FOXO1 antibody (diluted at 1:1000, Cell Signaling Technology), rabbit anti-phosphorylated p70 S6 kinase (S6K) antibody (diluted at 1:1000, Cell Signaling Technology), and rabbit anti-phosphorylated STAT3 antibody (diluted at 1:1000, Cell Signaling Technology). The membranes were then incubated with HRP-conjugated donkey anti-goat (diluted at 1:10,000, Jackson ImmunoResearch) or donkey anti-rabbit (diluted at 1:4,000, GE Healthcare) antibodies. Labeled proteins were detected with chemiluminescence using ECL detection reagent (GE Healthcare) according to the manufacturer's instructions. The membranes were exposed to hyperfilm ECL (GE Healthcare) for an appropriate period. The blotted membranes were stripped in 0.25 M of glycine, pH 2.5, at RT for 10 min and incubated with rat anti-tubulin antibody (diluted at 1:500; Abcam), rabbit anti-FOXO1 antibody (diluted at 1:1000, Cell Signaling Technology), rabbit anti-S6K antibody (diluted at 1:1000, Cell Signaling Technology), and rabbit anti-STAT3 antibody (diluted at 1:1000, Cell Signaling Technology) at 4 °C for 16 h followed by incubation with HRP-conjugated donkey anti-rat (diluted at 1:4000, Jackson ImmunoResearch) or donkey anti-rabbit antibodies (diluted at 1:4000, Jackson ImmunoResearch) at RT for 1 h.

Immunohistochemistry—Immunofluorescence staining was performed with some modifications as previously described (25). Briefly, the mice were deeply anesthetized with diethyl ether, and the epididymal adipose tissue was quickly removed. The adipose tissue was then fixed with 1% paraformaldehyde in PBS at 4 °C for 1 h followed by preincubation in 5% normal donkey serum at RT for 1 h. The adipose tissue was subsequently incubated with goat anti-OSMRβ antibody (diluted at 1:400), rat anti-F4/80 antibody (diluted at 1:1000; AbD Serotec), and rabbit anti-caveolin-1 antibody (diluted at 1:400; BD Biosciences). The adipose tissue was incubated with Cy2-conjugated, Cy3-conjugated, or biotinylated secondary antibodies (diluted at 1:800; Jackson ImmunoResearch) at RT for 1 h. The adipose tissue was then incubated with 7-amino-4-methylcoumarin-3-acetic acid-conjugated streptavidin (diluted at 1:500; Jackson ImmunoResearch) at RT for 30 min and mounted in mounting media (90% glycerol and 10% PBS) on the chambered slide. Immunofluorescence images were acquired using a confocal laser scanning microscope (LSM700; Carl Zeiss).

Immunohistochemical analysis of pancreas was performed as previously described (21). Briefly, 6-μm-thick frozen sections were treated with normal donkey serum and incubated with rabbit anti-insulin antibody (diluted at 1:400; Abcam). Then they were incubated with biotinylated donkey anti-rabbit IgG antibody (diluted at 1:800; Jackson ImmunoResearch) followed by the incubation with HRP-conjugated streptoavidin (DAKO, Carpinteria, CA). Thereafter, the peroxidase reaction was developed with 0.05% diaminobenzidine tetrahydrochloride (Sigma) and 0.01% H_2O_2. Eosin Y (Muto Pure Chemical, Tokyo, Japan) was used for counterstaining. Images were acquired by using a BIOREVO BZ-9000 microscope (KEYENCE, Osaka, Japan). To evaluate the area of β-cell in pancreas, every 20th section was selected from a series of consecutive pancreatic sections, and 12 sections per mouse were used for the analysis. For each section, the cells were considered to be positive for insulin if the cell bodies were stained brown. The area of β-cells and pancreas was quantified using Image J analysis software (Version 1.46r, Scion, Frederick, MD).

The following controls were performed: (i) incubation with protein A-purified goat or rabbit IgG instead of primary antibody; (ii) incubation without the primary antibody or without primary and secondary antibodies. All controls revealed no labeling (data not shown).

Measurement of Blood Glucose and Serum Insulin—Measurements of the blood glucose and serum insulin levels were obtained as previously described (21). The mice were fasted for 4 h to remove the effects of food intake on glucose metabolism, and blood was removed from the tail vein at 18:00 h. In the fasting experiments the mice were fasted overnight with free access to water. Serum was then immediately collected and stored at −20 °C. The blood glucose levels were measured with a glucose measurement device (Glucocard GT-1640, Arkray). The serum insulin concentrations were determined using kits from Morinaga.

Intraperitoneal Glucose Tolerance Tests (ipGTT) and Insulin Tolerance Tests (ITT)—ipGTT and ITT were performed as previously described (21). For the ipGTT, the mice were fasted for overnight, after which they received an intraperitoneal injection of D-glucose. Blood samples were collected from the tail vein before and at 15, 30, 60, and 120 min after the injection of D-glucose. For the ITT, the mice were fasted for 4 h, after which they received an intraperitoneal injection of human insulin. Blood samples were collected from the tail vein before and at 15, 30, 60, and 120 min after the injection of insulin.

ELISA—The concentrations of TNF-α, IL-10, and adiponectin were measured with ELISA kits (R & D Systems) according to the manufacturer's instructions. The serum leptin concentration was determined using an ELISA kit from Morinaga. The serum amyloid A concentration was measured with an ELISA kit from Invitrogen.

Measurement of the Lipid Content in the Serum and Liver—The serum levels of triglycerides, total cholesterol, and free fatty acids were measured at Nagahama Life Science Laboratory using lipid assay kits (Triglyceride E-Test Wako, Total Cholesterol E-Test Wako, and NEFA C-Test Wako, Wako Pure Chemical Industries) according to the manufacturer's instructions. The content of triglycerides and total cholesterol in the liver was analyzed at Skylight Biotech (Akita, Japan).

As described previously (21), the mice were fasted for 4 h to remove the effects of food intake on lipid metabolism, and liver

−674−
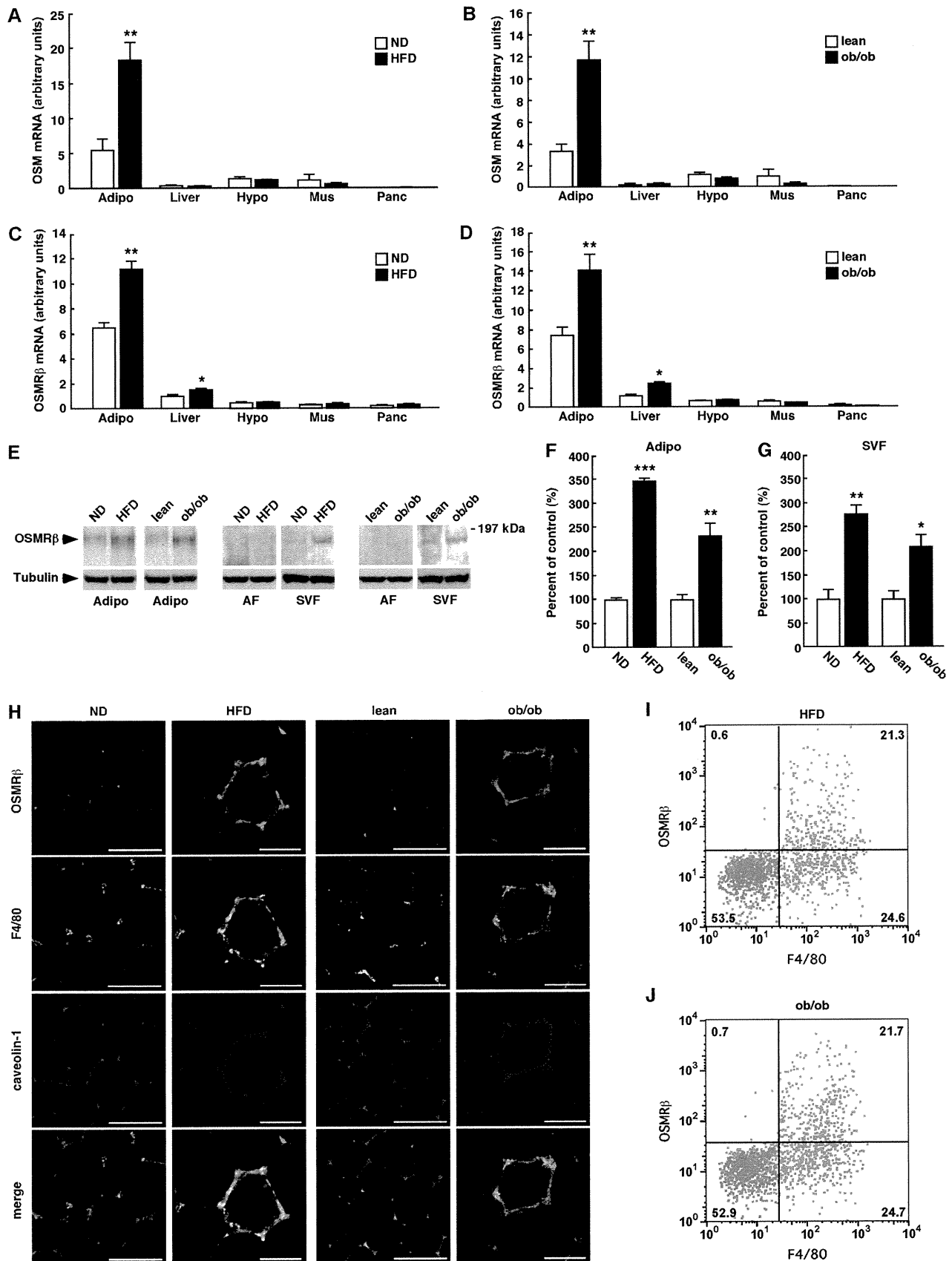
was dissected at 15:00 h. In the fasting experiments the mice were fasted for overnight with free access to water. Lipids were extracted from the liver according to the Folch method (26). The frozen liver tissues were homogenized, and triglycerides and total cholesterol were extracted from the homogenate with chloroform/methanol (2:1, v/v), dried, and resuspended in 2-propanol. The amounts of triglycerides and total cholesterol in the extract were measured using lipid assay kits (Cholestest TG and Cholestest CHO, Sekisui Medical).

Quantitative Real-time PCR—Quantitative real-time PCR was performed with some modifications, as previously described (25). Briefly, total RNA extracted from epididymal adipose tissue, SVF, liver, hypothalamus, skeletal muscle, and pancreas was prepared using TRI reagent (Molecular Research Center). The cDNA from the total RNA was synthesized with TaqMan Reverse Transcription Reagents (Applied Biosystems). The following Taq-Man Gene Expression Assays (Applied Biosystems) were used: OSM (Mm01193966_m1), OSMRβ (Mm00495424_m1), insulin (P/N4323969), TNF-α (Mm00443258_m1), IL-1β (Mm00434228_m1), interferon-γ (IFN-γ) (Mm00801778_m1), monocyte chemoattractant protein-1 (MCP-1) (Mm00441242_m1), C-C chemokine receptor 2 (CCR2) (Mm00438270_m1), toll-like receptor 4 (TLR4) (Mm00445273_m1), IL-6 (Mm00446190_m1), IL-10 (Mm00439616_m1), IL-13 (Mm00434204_m1), adiponectin (Mm00456425_m1), macrophage galactose-type C-type lectin 1 (MGL1) (Mm00546124_m1), MGL2 (Mm00460844_m1), fatty-acid synthase (FAS) (Mm00662319_m1), stearoyl CoA desaturase-1 (SCD-1) (Mm00772290_m1), sterol regulatory-element binding transcription factor-1 (SREBF-1) (Mm00550338_m1), ACSL3 (Mm01255804_m1), ACSL5 (Mm01261083_m1), and 18S (Hs99999901_s1). Quantitative real-time PCR of each gene was performed using Rotor Gene Q (Qiagen) and Rotor Gene Probe PCR kits (Qiagen). The PCR amplification protocol was as follows: 95 °C for 10 min followed by 40 cycles of 95 °C for 10 s and 60 °C for 45 s. The relative abundance of transcripts was normalized according to the expression of 18 S mRNA and analyzed using the ΔΔCT method.

Statistical Analysis—The results are presented as the mean ± S.E. Statistically significant differences between groups were analyzed using Student's t test or an analysis of variance followed by the post-hoc Bonferroni test. The criterion for statistical significance was a p value of < 0.05.

RESULTS

Expression of OSMRβ in the Adipose Tissue of the Obese Mice—We previously reported that OSMRβ is expressed in adipose tissue, especially in the ATMs of C57BL/6J mice under normal dietary conditions (21). We first investigated the expression levels of OSM and OSMRβ in various tissues of two types of obese model mice, DIO mice and genetically obese *ob/ob* mice. In non-obese mice, both OSM and OSMRβ were abundantly expressed in the adipose tissue (Fig. 1, *A–D*). The expression of OSM only increased in the adipose tissues of both types of obese model mice (Fig. 1, *A* and *B*). In contrast, the OSMRβ expression was increased in the adipose tissue and liver but not in the hypothalamus, skeletal muscle, and pancreas in the obese mice (Fig. 1, *C* and *D*). In the adipose tissue, the expression of OSMRβ was predominantly increased in the SVF in DIO and *ob/ob* mice compared with that observed in the respective control mice (Fig. 1, *E–G*). However, OSMRβ was rarely detected in the adipocyte fraction of all mice examined (Fig. 1*E*). Immunofluorescence staining revealed that OSMRβ was expressed in F4/80-positive macrophages in the adipose tissue of the DIO and *ob/ob* mice and the respective control mice (Fig. 1*H*). However, the intensity of staining for OSMRβ in macrophages and the number of OSMRβ-positive macrophages were increased in the adipose tissue in the DIO and *ob/ob* mice compared with those observed in the respective control mice (Fig. 1*H*). Flow cytometric analysis revealed that OSMRβ was exclusively expressed in F4/80-positive macrophages in the adipose tissue of both the DIO (97.0 ± 1.1%; Fig. 1*I*) and *ob/ob* mice (96.7 ± 0.3%; Fig. 1*J*). In addition, almost half of F4/80-positive macrophages was OSMRβ-positive in the adipose tissue of the DIO (45.0 ± 1.1%; Fig. 1*I*) and *ob/ob* mice (43.8 ± 1.7%; Fig. 1*J*).

OSMRβ$^{-/-}$ Mice Develop Obesity and Insulin Resistance under HFD Conditions—To investigate the roles of OSM signaling in the development of obesity-induced metabolic disorders, we fed 8-week-old OSMRβ$^{-/-}$ mice and WT littermates an HFD for 8 weeks. As the amount of food intake and the food intake per body weights were increased in OSMRβ$^{-/-}$ mice compared with that observed in WT mice under HFD conditions (Fig. 2, *D* and *E*), we conducted a pair-feeding study to investigate the effects of food intake on metabolic parameters in OSMRβ$^{-/-}$ mice. Remarkably, OSMRβ$^{-/-}$ mice began to gain more weight than WT mice at 4 weeks on the HFD and remained heavier until 8 weeks on the HFD (Fig. 2, *A* and *B*). In OSMRβ$^{-/-}$ mice pair-fed with WT mice, designated OSMRβ$^{-/-}$(PF) mice, the body weight values were similar to those in WT mice (Fig. 2, *A* and *B*). The weights of the adipose tissues (epididymal and subcutaneous) of OSMRβ$^{-/-}$ mice were heavier than those of WT and OSMRβ$^{-/-}$(PF) mice at 8 weeks on the HFD (Fig. 2C). Consistent with these data, the serum concentration of leptin in OSMRβ$^{-/-}$ mice was higher


FIGURE 1. **The expressions of OSM and OSMRβ in various tissues of non-obese and obese mice.** *A* and *B*, the mRNA expressions of OSM in the adipose tissue, liver, hypothalamus, skeletal muscle, and pancreas in the WT mice fed a normal diet (*ND*) or a HFD (*A*) and the lean and *ob/ob* mice (*B*) (*n* = 6). *C* and *D*, the mRNA expressions of OSMRβ in the adipose tissue, liver, hypothalamus, skeletal muscle, and pancreas in the WT mice fed a ND or an HFD (*C*) and the WT and *ob/ob* mice (*D*) (*n* = 6). *E*, Western blot analysis of OSMRβ in the adipose tissues of the non-obese and obese mice. The apparent molecular masses are indicated on the *right*. Bands corresponding to OSMRβ were detected at 180 kDa. *F* and *G*, a quantitative analysis of the protein expression of OSMRβ in the entire adipose tissue specimen (*F*) and SVF (*G*) (*n* = 6). *H*, immunofluorescence staining for OSMRβ (*red*) with F4/80 (*green*) and caveolin-1 (*blue*) in the adipose tissues of the obese mice and the respective controls. *Scale bar* = 100 μm. *I* and *J*, the expression of OSMRβ and F4/80 in SVF cells analyzed by flow cytometry. Isolated SVF cells from the adipose tissue of DIO (*I*) and *ob/ob* mice (*J*) were stained with antibodies against F4/80 and OSMRβ (*blue dots*). *Red dots* show the data with their control antibodies (*n* = 4). *ND*, C57BL/6J mice fed a normal diet at 16 weeks old; *HFD*, C57BL/6J mice fed an HFD for 8 weeks started at 8 weeks old; *lean*, control for *ob/ob* mice at 8 weeks old; *ob/ob*, *ob/ob* mice at 8 weeks old; *Adipo*, adipose tissue; *AF*, adipocyte fraction; *Hypo*, hypothalamus; *Mus*, skeletal muscle; *Panc*, pancreas. The data represent the mean ± S.E. *, $p < 0.05$; **, $p < 0.01$; ***, $p < 0.005$ normal diet (*ND*) *versus* HFD or lean *versus ob/ob*, Student's *t* test.

than that observed in WT and OSMRβ$^{-/-}$(PF) mice (Table 1). However, the serum concentration of adiponectin did not differ between the three groups (Table 1).

The blood glucose concentration in OSMRβ$^{-/-}$ and OSMRβ$^{-/-}$(PF) mice began to increase compared with those observed in WT mice after 6 weeks on the HFD (Fig. 2F), whereas the serum insulin concentration in OSMRβ$^{-/-}$ and

OSMRβ$^{-/-}$(PF) mice began to increase after 1 week on the HFD and continued to increase for 8 weeks (Fig. 2G). After 8 weeks on the HFD, the concentrations of blood glucose and serum insulin were increased in OSMRβ$^{-/-}$ and OSMRβ$^{-/-}$(PF) mice compared with those observed in WT mice under both fed and fasted states (Table 1). There were no significant differences in the concentrations of blood glucose and serum insulin between
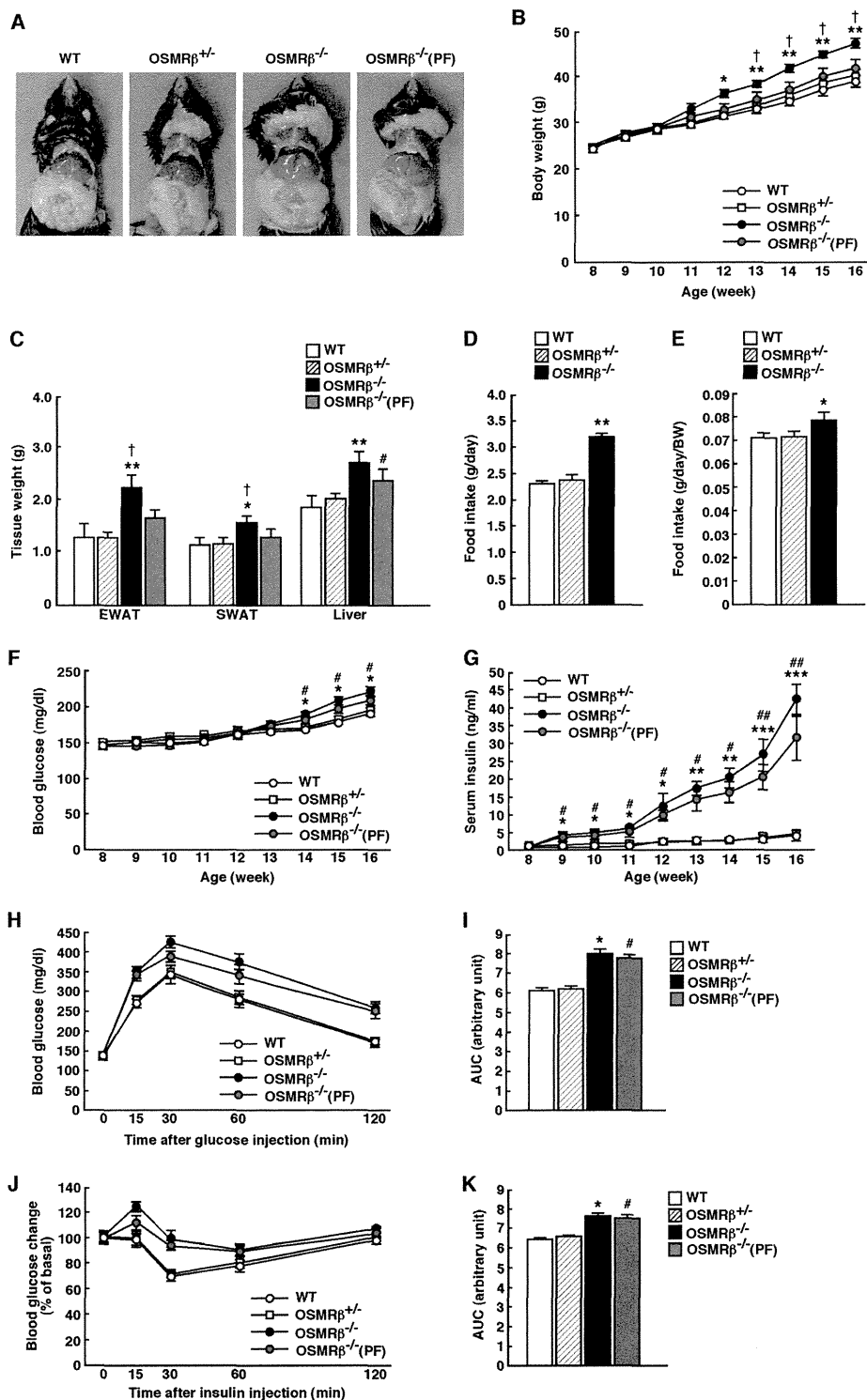
TABLE 1
Various metabolic parameters in the serum of WT and OSMRβ$^{-/-}$ mice under HFD conditions ($n = 6-8$)
In the fed states, mice were fasted for 4 h before the experiments to eliminate the feeding effect on lipid metabolism. In the fasted states, mice were fasted for overnight before the experiments. The data represent the mean ± S.E.

Serum concentration	WT	OSMRβ$^{-/-}$	OSMRβ$^{-/-}$(PF)
Leptin (ng/ml)	19.0 ± 2.2	25.7 ± 1.3^{a,b}	22.6 ± 1.8
Serum amyloid A (ng/ml)	26.9 ± 7.0	69.3 ± 15.8^{a}	46.8 ± 9.1^{c}
TNF-α (pg/ml)	5.80 ± 0.32	6.41 ± 0.23^{a}	6.13 ± 0.18
IL-10 (pg/ml)	11.7 ± 1.1	14.4 ± 0.5^{a}	12.9 ± 1.5
Adiponectin (μg/ml)	22.8 ± 0.1	22.9 ± 0.8	22.6 ± 1.8
Glucose (fed) (mg/dl)	163.7 ± 17.2	235.3 ± 8.3^{d}	203.8 ± 16.9^{c}
Glucose (fasted) (mg/dl)	119.3 ± 3.5	126.3 ± 1.9^{a}	125.8 ± 3.3^{c}
Insulin (fed) (ng/ml)	4.14 ± 1.42	42.0 ± 4.5^{a}	36.4 ± 6.2^{c}
Insulin (fasted) (ng/ml)	1.73 ± 2.81	20.0 ± 3.8^{a}	16.3 ± 8.2^{c}
Total cholesterol (fed) (mg/dl)	153.8 ± 11.6	200.3 ± 17.3^{a}	186.2 ± 19.6^{c}
Total cholesterol (fasted) (mg/dl)	70.0 ± 6.3	104.8 ± 7.7^{a}	Not tested
Triglyceride (fed) (mg/dl)	147.0 ± 12.6	175.5 ± 13.6^{a}	164.0 ± 6.4^{c}
Triglyceride (fasted) (mg/dl)	22.0 ± 1.9	36.0 ± 6.6^{a}	Not tested
Free fatty acid (fed) (mmol/liter)	1.76 ± 0.09	1.90 ± 0.13	1.90 ± 0.08
Free fatty acid (fasted) (mmol/liter)	0.75 ± 0.04	0.83 ± 0.05	Not tested

^{a} $p < 0.05$ WT *versus* OSMRβ$^{-/-}$ mice, Student's t test.
^{b} $p < 0.05$ OSMRβ$^{-/-}$ *versus* OSMRβ$^{-/-}$ (PF) mice, Student's t test.
^{c} $p < 0.05$ WT *versus* OSMRβ$^{-/-}$ (PF) mice, Student's t test.
^{d} $p < 0.01$ WT *versus* OSMRβ$^{-/-}$ mice, Student's t test.

OSMRβ$^{-/-}$ and OSMRβ$^{-/-}$(PF) mice (Table 1). The ipGTTs and ITTs demonstrated that glucose tolerance and insulin sensitivity were reduced in OSMRβ$^{-/-}$ mice compared with those observed in WT mice at 8 weeks on the HFD, as measured by the area under the curves (AUCs) of blood glucose on the ipGTTs and ITTs (Fig. 2, *H–K*). There were no significant differences in the AUCs of blood glucose between OSMRβ$^{-/-}$ and OSMRβ$^{-/-}$(PF) mice (Fig. 2, *I* and *K*). There were no significant differences in the body weights, tissue weights, food intake, blood glucose, and serum insulin between WT and heterozygous OSMRβ-deficient mice (OSMRβ$^{+/-}$ mice) under HFD conditions (Fig. 2).

Similar to the data obtained from the male mice, the body weights, tissue weights, and the level of food intake were also increased in the female OSMRβ$^{-/-}$ mice fed the HFD compared with those observed in female WT mice fed the HFD (Fig. 3, *A–D*). In addition, the female OSMRβ$^{-/-}$ mice fed the HFD exhibited more severe glucose intolerance than female WT mice fed the HFD, as measured on the ipGTTs (Fig. 3, *E* and *F*).

OSMRβ$^{-/-}$ Mice Exhibit Severe Hepatic Steatosis under HFD Conditions—The liver weight in OSMRβ$^{-/-}$ mice, which was not significantly different from that in OSMRβ$^{-/-}$(PF) mice, was heavier than that in WT mice (Fig. 2*C*). To detect intracellular lipid droplets and glycogen granules in the liver, we performed Oil Red O and periodic acid-Schiff (PAS) staining, respectively. The Oil Red O staining revealed that lipid accumulation was augmented in the livers of OSMRβ$^{-/-}$ and OSMRβ$^{-/-}$(PF) mice compared with that observed in WT mice (Fig. 4*A*). In contrast, the PAS staining showed that there

were fewer glycogen granules in the hepatocytes of OSMRβ$^{-/-}$ and OSMRβ$^{-/-}$(PF) mice compared with those observed in WT mice (Fig. 4*A*). Consistent with these data, the serum concentrations of total cholesterol and triglyceride were increased in OSMRβ$^{-/-}$ and OSMRβ$^{-/-}$(PF) mice compared with those observed in WT mice in both fed and fasted states (Table 1). There was a tendency for the serum concentration of free fatty acids to be increased in OSMRβ$^{-/-}$ and OSMRβ$^{-/}$$^{-}$(PF) mice compared with that observed in WT mice in both fed and fasted states; however, their differences were not statistically significant (Table 1). In addition, the total cholesterol and triglyceride levels in the livers of OSMRβ$^{-/-}$ and OSMRβ$^{-/-}$(PF) mice were higher than those observed in WT mice (Fig. 4, *B* and *C*). To provide insight into the cause of the increased lipid accumulation observed in the livers of OSMRβ$^{-/-}$ and OSMRβ$^{-/-}$(PF) mice, we investigated the expression levels of genes related to fatty acid synthesis in the liver. The expression levels of FAS, SCD-1, and SREBF-1 were increased in the livers of OSMRβ$^{-/-}$ and OSMRβ$^{-/-}$(PF) mice compared with those observed in the liver of WT mice (Fig. 4*D*). In addition, phosphorylation of S6K, which increases the activity of SREBF-1 (27), was up-regulated in the liver of OSMRβ$^{-/-}$ and OSMRβ$^{-/-}$(PF) mice (Fig. 4, *E* and *F*). Thus, severe hepatic steatosis concomitant with enhanced S6K activation and increased lipogenic gene expression was observed in the liver of OSMRβ$^{-/-}$ mice.

Impaired Insulin Signaling in OSMRβ$^{-/-}$ Mice under HFD Conditions—To evaluate insulin signaling pathways in adipose tissue, skeletal muscle, and liver, we investigated the phosphor-

FIGURE 2. **Body weight and glucose metabolism in WT and OSMRβ$^{-/-}$ mice under HFD conditions.** The mice (8 weeks old) were fed an HFD for 8 weeks. *A*, representative images of WT mice, OSMRβ$^{+/-}$ mice, OSMRβ$^{-/-}$ mice, and OSMRβ$^{-/-}$ mice pair-fed with WT mice (*PF*). *B*, the body weights of WT, OSMRβ$^{+/-}$, OSMRβ$^{-/-}$, and OSMRβ$^{-/-}$(PF) mice ($n = 6-11$). *C*, the tissue weights in WT, OSMRβ$^{+/-}$, OSMRβ$^{-/-}$, and OSMRβ$^{-/-}$(PF) mice at 8 weeks on the HFD ($n = 6-11$). *EWAT*, epididymal white adipose tissue; *SWAT*, subcutaneous white adipose tissue. *D*, the amount of food intake in WT, OSMRβ$^{+/-}$, OSMRβ$^{-/-}$, and OSMRβ$^{-/-}$(PF) mice at 8 weeks on the HFD ($n = 6-11$). *E*, the amount of food intake per body weights in WT, OSMRβ$^{+/-}$, OSMRβ$^{-/-}$, and OSMRβ$^{-/-}$(PF) mice at 8 weeks on the HFD ($n = 6-11$). *F* and *G*, the blood glucose (*F*) and serum insulin (*G*) levels in WT, OSMRβ$^{+/-}$, OSMRβ$^{-/-}$, and OSMRβ$^{-/-}$(PF) mice in the fed state ($n = 6$). In the fed states, mice were fasted for 4 h before the experiments to eliminate the feeding effects on glucose metabolism. *H–K*, the results of the ipGTTs (*H*) and ITTs (*J*) in WT, OSMRβ$^{+/-}$, OSMRβ$^{-/-}$, and OSMRβ$^{-/-}$(PF) mice at 8 weeks on the HFD ($n = 6$). For ipGTTs, mice were fasted for 16 h and intraperitoneally injected with D-glucose (1 g/kg of body weight). For ITTs, mice were fasted for 4 h and intraperitoneally injected with insulin (1 unit/kg of body weight). The AUC for blood glucose on the ipGTTs (*I*) and ITTs (*K*) is shown. The data represent the mean ± S.E. *, $p < 0.05$; **, $p < 0.01$; ***, $p < 0.005$ WT *versus* OSMRβ$^{-/-}$ mice; #, $p < 0.05$; ##, $p < 0.01$ WT *versus* OSMRβ$^{-/-}$(PF) mice; †, $p < 0.05$ OSMRβ$^{-/-}$ *versus* OSMRβ$^{-/-}$(PF) mice, analysis of variance followed by the post-hoc Bonferroni test (*B, F*, and *G*); Student's t test (*C, D, E, I*, and *K*).
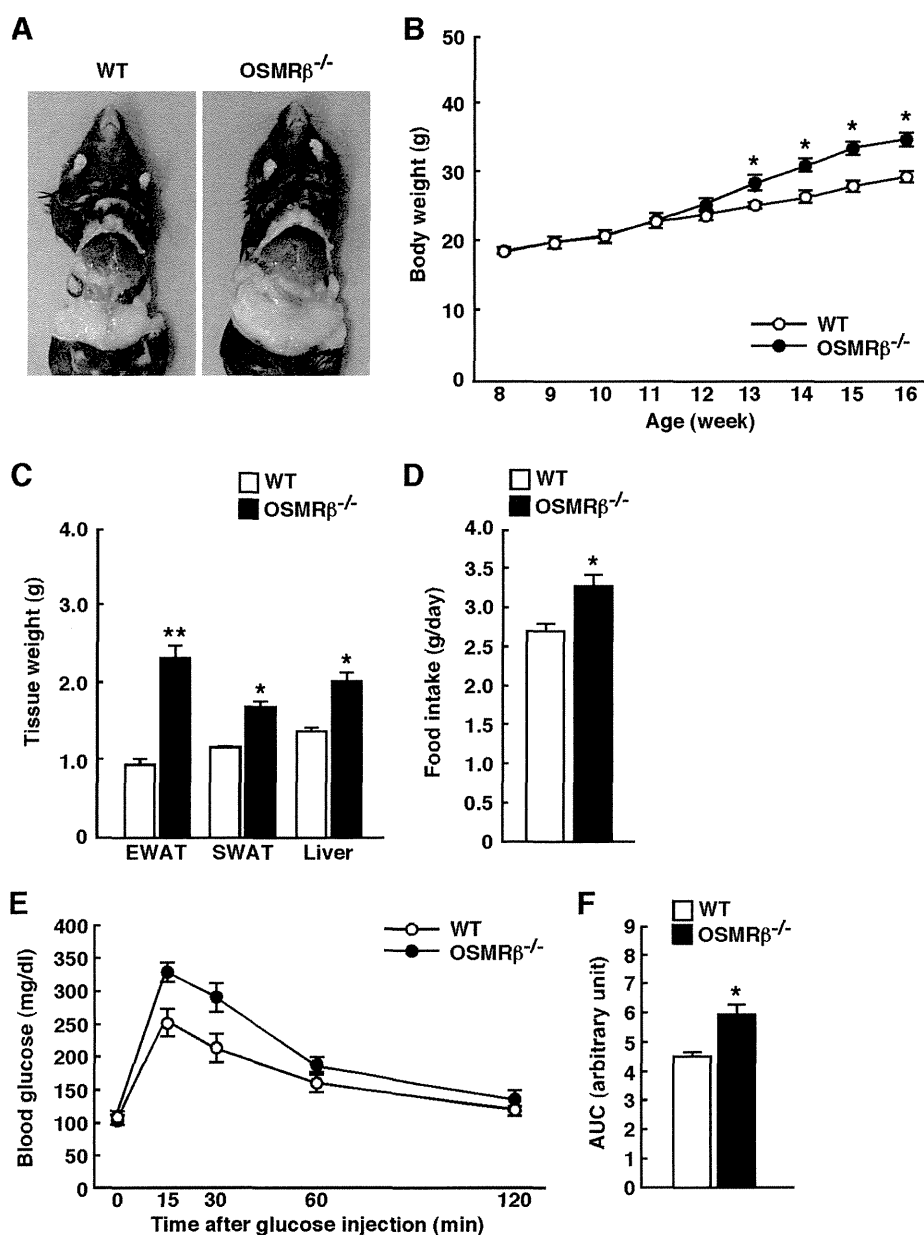
FIGURE 3. **Body weights and glucose metabolism in the female WT and OSMRβ$^{-/-}$ mice under HFD conditions.** The mice (8 weeks old) were fed an HFD for 8 weeks. *A*, representative images of the female WT and OSMRβ$^{-/-}$ mice. *B*, the body weights of the female WT and OSMRβ$^{-/-}$ mice (*n* = 6). *C*, the tissue weights in the female WT and OSMRβ$^{-/-}$ mice at 8 weeks on the HFD (*n* = 6). *EWAT*, epididymal white adipose tissue; *SWAT*, subcutaneous white adipose tissue. *D*, the amount of food intake in the female WT and OSMRβ$^{-/-}$ mice (*n* = 6). *E* and *F*, the results of the ipGTTs in the female WT and OSMRβ$^{-/-}$ mice at 8 weeks on the HFD (*n* = 6). For ipGTTs, mice were fasted for 16 h and intraperitoneally injected with D-glucose (1 g/kg of body weight). The AUC for glucose on the ipGTTs (*F*) is shown. The data represent the mean ± S.E. *, *p* < 0.05; **, *p* < 0.01 WT *versus* OSMRβ$^{-/-}$ mice, analysis of variance followed by the post-hoc Bonferroni test (*B*); Student's *t* test (*C*, *D*, and *F*).

ylation level of Akt induced by the stimulation with insulin in each tissue. Without the stimulation with insulin, phosphorylation of Akt was hardly observed in the adipose tissue, skeletal muscle, and liver of WT, OSMRβ$^{-/-}$, and OSMRβ$^{-/-}$(PF) mice in the fasted states (data not shown). After the stimulation with insulin, Akt was phosphorylated in the adipose tissue, skeletal muscle, and liver of these mice (Fig. 5A). However, the level of insulin-induced Akt phosphorylation was decreased in the adipose tissue, skeletal muscle, and liver of OSMRβ$^{-/-}$ and OSMRβ$^{-/-}$(PF) mice compared with that observed in WT mice (Fig. 5B).

Next, we examined the phosphorylation level of FOXO1 and S6K, which are important for the suppression of gluconeogenesis (28) and the activation of lipogenesis (29), respectively, in the liver. Without the stimulation with insulin, phosphorylation of FOXO1 and S6K was hardly observed in the liver of WT, OSMRβ$^{-/-}$, and OSMRβ$^{-/-}$(PF) mice in the fasted state (data not shown). After the stimulation with insulin, FOXO1 and S6K were phosphorylated in the livers of these mice (Fig. 5, *C–F*). In addition, phosphorylation level of FOXO1 was decreased in the liver of OSMRβ$^{-/-}$ and OSMRβ$^{-/-}$(PF) mice compared with that observed in WT mice (Fig. 5D). In contrast, phosphoryla-
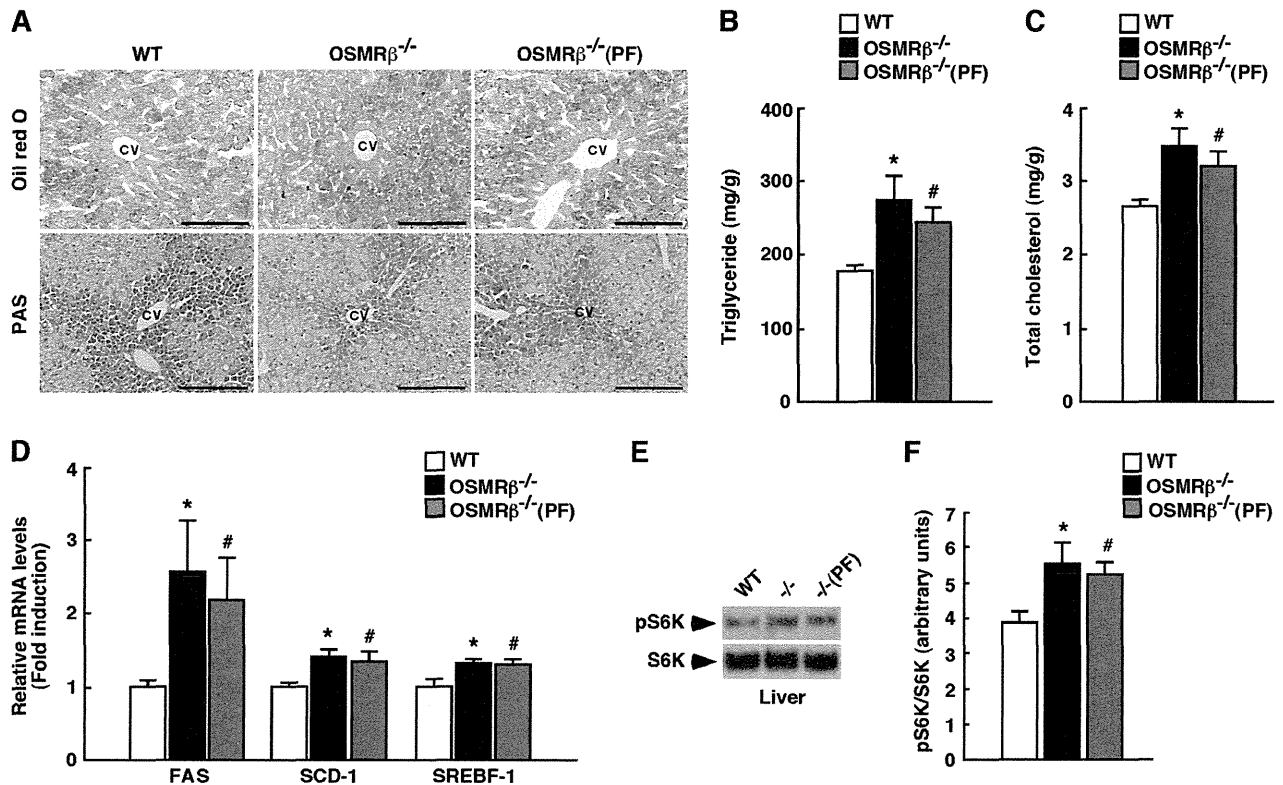
FIGURE 4. **Lipid metabolism in the livers of WT and OSMRβ$^{-/-}$ mice under HFD conditions.** The mice (8 weeks old) were fed an HFD for 8 weeks. A, Oil Red O and PAS staining of the livers of WT, OSMRβ$^{-/-}$, and OSMRβ$^{-/-}$(PF) mice. CV, central vein. Scale bar = 100 μm. B and C, the content of triglycerides (B) and total cholesterol (C) in the livers of WT, OSMRβ$^{-/-}$, and OSMRβ$^{-/-}$(PF) mice in the fed state ($n = 6$). D, the expression levels of genes related to fatty acid synthesis (FAS, SCD-1, and SREBF-1) in the livers of WT, OSMRβ$^{-/-}$, and OSMRβ$^{-/-}$(PF) mice in the fed state ($n = 6$). E, Western blot analysis of phosphorylation of S6K (pS6K) in the livers of WT, OSMRβ$^{-/-}$, and OSMRβ$^{-/-}$(PF) mice in the fed state. F, a quantitative analysis of pS6K ($n = 6$). In the fed state, mice were fasted for 4 h before the experiments to eliminate the feeding effects on lipid metabolism. The data represent the mean ± S.E. *, $p < 0.05$ WT versus OSMRβ$^{-/-}$ mice; #, $p < 0.05$ WT versus OSMRβ$^{-/-}$(PF) mice, Student's t test.

tion of S6K in OSMRβ$^{-/-}$ and OSMRβ$^{-/-}$(PF) mice was maintained at the same levels as that observed in WT mice (Fig. 5F), suggesting that insulin signaling pathway related to lipogenesis was preserved in the liver of OSMRβ$^{-/-}$ mice.

OSMRβ$^{-/-}$ Mice Exhibit Hyperplasia of β-Cells in Pancreas under HFD Conditions—Histological examination of the pancreas revealed that the percentages of insulin-positive areas (β-cells) among total areas of the pancreas were higher in OSMRβ$^{-/-}$ and OSMRβ$^{-/-}$(PF) mice compared with those observed in WT mice (Fig. 5, G and H), suggesting that OSMRβ$^{-/-}$ mice exhibit hyperplasia of β-cells in the pancreas. In addition, the expression of insulin mRNA was increased in the pancreas of OSMRβ$^{-/-}$ and OSMRβ$^{-/-}$(PF) mice compared with that in WT mice (Fig. 5I).

HFD Conditions Exacerbate Adipose Tissue Inflammation in OSMRβ$^{-/-}$ Mice—The serum concentrations of TNF-α, IL-10, and serum amyloid A were higher in OSMRβ$^{-/-}$ and OSMRβ$^{-/-}$(PF) mice than those observed in WT mice at 8 weeks on the HFD (Table 1), indicating that the degree of systemic inflammation was elevated in OSMRβ$^{-/-}$ and OSMRβ$^{-/-}$(PF) mice. In the adipose tissue, the total number of F4/80-positive macrophages per weight of adipose tissue was higher in OSMRβ$^{-/-}$ and OSMRβ$^{-/-}$(PF) mice than those observed in WT mice (Fig. 6A). The percentages of both CD11c-positive M1-type macrophages and CD206-positive

M2-type macrophages among the total number of F4/80-positive macrophages were higher in the adipose tissue of OSMRβ$^{-/-}$ and OSMRβ$^{-/-}$(PF) mice than in those of WT mice (Fig. 6, B and C). The percentages of CD11c/CD206-double-negative cells among the total number of F4/80-positive macrophages were lower in the adipose tissue of OSMRβ$^{-/-}$ and OSMRβ$^{-/-}$(PF) mice than in those of WT mice (Fig. 6D). In addition, the expression levels of inflammatory markers, including TNF-α, IL-1β, IFN-γ, MCP-1, CCR2, and TLR4, were higher in the adipose tissue and SVF of OSMRβ$^{-/-}$ and OSMRβ$^{-/-}$(PF) mice than those observed in WT mice, whereas there were no differences in the IL-6 expression levels between the three groups (Fig. 6, E and F). In contrast, the adiponectin expression level was lower in the adipose tissue and SVF of OSMRβ$^{-/-}$ and OSMRβ$^{-/-}$(PF) mice than in those of WT mice (Fig. 6, E and F). Unexpectedly, the expression levels of other anti-inflammatory markers, including IL-10, IL-13, MGL1, and MGL2, were also higher in the adipose tissue and SVF of OSMRβ$^{-/-}$ and OSMRβ$^{-/-}$(PF) mice than in those of WT mice (Fig. 6, E and F).

To determine whether the increases in anti-inflammatory markers were secondary to the preceding inflammatory response, we investigated the development of adipose tissue inflammation in OSMRβ$^{-/-}$ mice at the earlier stage. At 4 weeks on the HFD (Fig. 7, A and B), the total number of
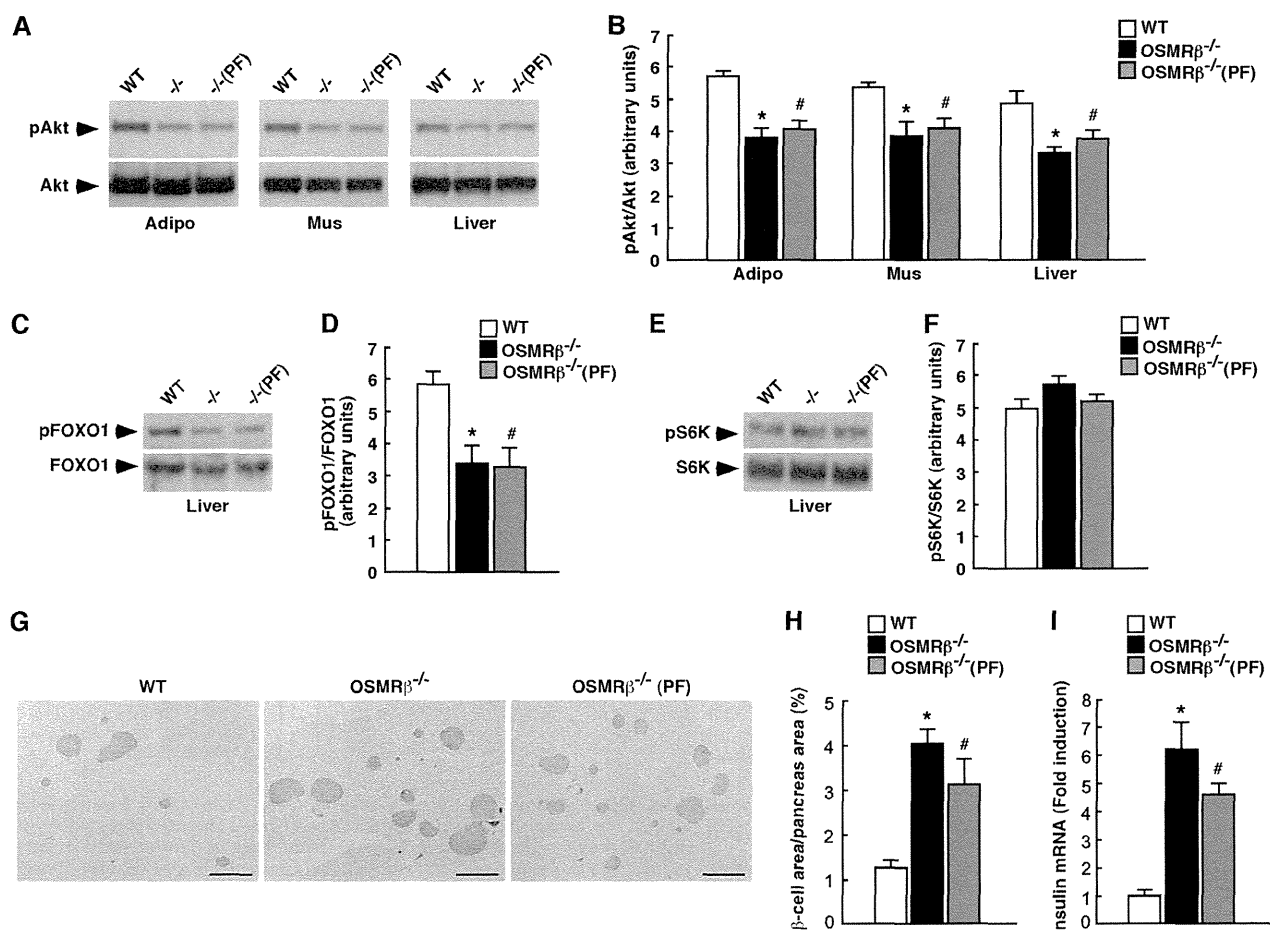
FIGURE 5. **Insulin signaling pathways in WT and OSMRβ$^{-/-}$ mice at 8 weeks on the HFD.** After 24 h of fasting, mice were intraperitoneally injected with insulin (10 milliunits/g of body weight) and maintained for 10 min. *A*, insulin-stimulated Akt phosphorylation in the adipose tissues, skeletal muscles, and livers of WT, OSMRβ$^{-/-}$, and OSMRβ$^{-/-}$ (PF) mice ($n = 6$). *B*, a quantitative analysis of pAkt ($n = 6$). *C–F*, insulin-stimulated phosphorylation of FOXO1 (*pFOXO1*) (*C*) and S6K (*pS6K*) (*E*) in the livers of WT, OSMRβ$^{-/-}$, and OSMRβ$^{-/-}$ (PF) mice. A quantitative analysis of pFOXO1 (*D*) and pS6K (*F*) ($n = 6$) is shown. *G*, immunohistochemistry for insulin in the pancreas of WT, OSMRβ$^{-/-}$, and OSMRβ$^{-/-}$ (PF) mice. *Scale bars* = 500 μm. *H*, quantitative analysis of the area of β-cells in the total area of the pancreas. *I*, the mRNA expression of insulin in the pancreas of WT, OSMRβ$^{-/-}$, and OSMRβ$^{-/-}$ (PF) mice in the fed states. *Adipo*, adipose tissue; *Mus*, skeletal muscle. The data represent the mean ± S.E. *, $p < 0.05$ WT *versus* OSMRβ$-/-$ mice; #, $p < 0.05$ WT *versus* OSMRβ$^{-/-}$ (PF) mice; Student's *t* test.

F4/80-positive macrophages per weight of adipose tissue and the percentage of CD11c-positive M1-type macrophages were increased in OSMRβ$^{-/-}$ mice compared with those observed in WT mice. In addition, the expression levels of inflammatory markers, including TNF-α, IL-1β, IFN-γ, MCP-1, CCR2, and TLR4, were higher in the adipose tissue and SVF of OSMRβ$^{-/-}$ mice than in those of WT mice at 4 weeks on the HFD (Fig. 7, *E* and *F*). In contrast, the percentage of CD206-positive M2-type macrophages was decreased in the adipose tissue of OSMRβ$^{-/-}$ mice compared with that observed in WT mice at 4 weeks on the HFD (Fig. 7*C*). In addition, the expression levels of anti-inflammatory markers, including IL-10, IL-13, MGL1, and MGL2, were lower in the adipose tissue and SVF of OSMRβ$^{-/-}$ mice than in those of WT mice at 4 weeks on the HFD (Fig. 7, *E* and *F*). There were no differences in the expression levels of IL-6 and adiponectin in the adipose tissue between WT and OSMRβ$^{-/-}$ mice (Fig. 7, *E* and *F*). Such changes in the total number of ATMs, the polarization of ATMs, and cytokine production profiles were already observed in OSMRβ$^{-/-}$ mice at 2

weeks on the HFD, when there was no difference in body weight between WT and OSMRβ$^{-/-}$ mice (Fig. 7, *A–F*). There were no differences in the percentages of CD11c/CD206-double-negative cells among the total number of F4/80-positive macrophages in the adipose tissue between WT and OSMRβ$^{-/-}$ mice at both 2 and 4 weeks on the HFD (Fig. 7*D*). Both glucose intolerance and insulin resistance were exacerbated in OSMRβ$^{-/-}$ mice compared with those observed in WT mice at both 2 and 4 weeks on the HFD (Fig. 7, *G–N*). Therefore, the increases in the levels of anti-inflammatory markers observed at 8 weeks on the HFD were considered to reflect a secondary response to an earlier inflammatory reaction in the adipose tissue of OSMRβ$^{-/-}$ mice.

Treatment with OSM Improves Insulin Resistance, Adipose Tissue Inflammation, and Hepatic Steatosis in Genetically Obese ob/ob Mice—To assess the effects of OSM on insulin resistance, adipose tissue inflammation, and hepatic steatosis in obese mice, OSM was intraperitoneally injected into *ob/ob* mice twice a day for 7 days. The body weights, adipose tissue weights, and liver weights were decreased in the OSM-treated